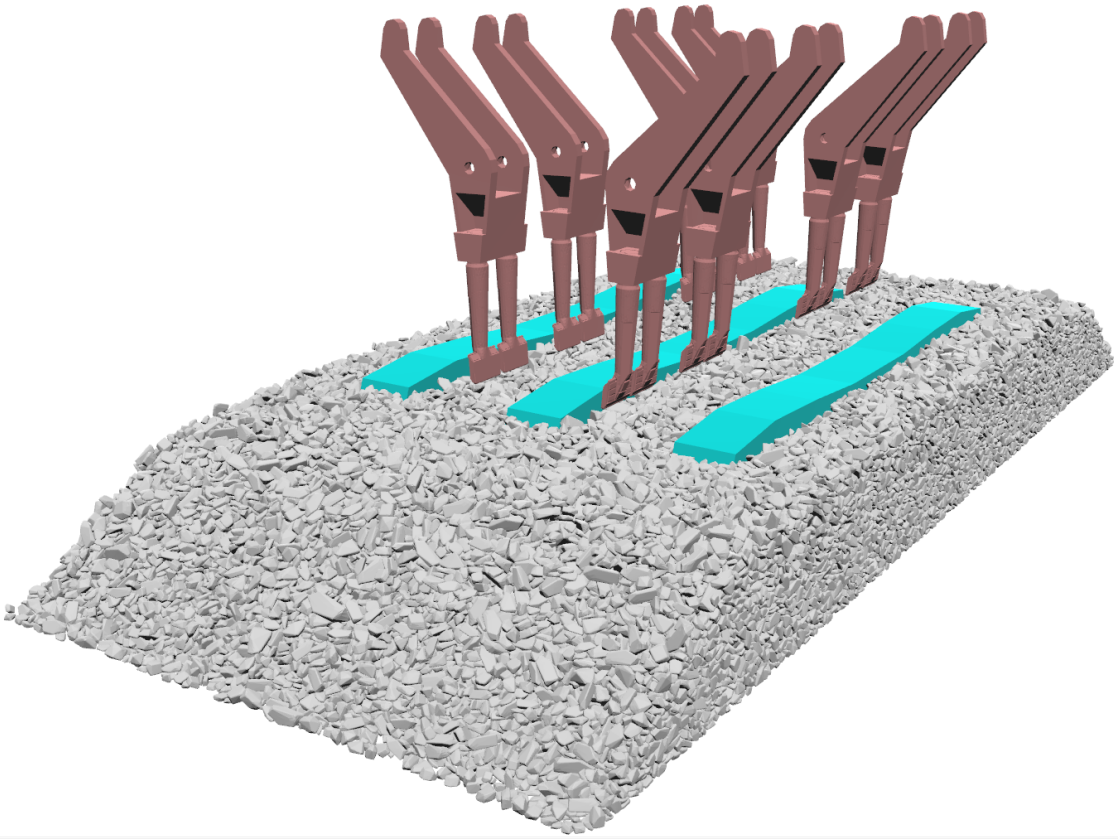

Numerical analysis of railway ballast tamping using a DEM-MBD co-simulation framework

Master's thesis in Applied Mechanics

Pontus Malmsköld

DEPARTMENT OF INDUSTRIAL AND MATERIALS SCIENCE
CHALMERS UNIVERSITY OF TECHNOLOGY
Gothenburg, Sweden 2024
www.chalmers.se

Master's thesis 2024

Numerical analysis of railway ballast tamping using a DEM-MBD co-simulation framework

Pontus Malmsköld

CHALMERS
UNIVERSITY OF TECHNOLOGY

Department of Industrial and Materials Science
Division of Material & Computational Mechanics
Chalmers University of Technology
Gothenburg, Sweden 2024

Numerical analysis of railway ballast tamping using a DEM-MBD co-simulation framework
Pontus Malmsköld

Supervisor: Johannes Quist and Anita Ullrich, Fraunhofer-Chalmers Centre
Examiner: Fredrik Larsson, Department of Industrial and Materials Science

Master's Thesis 2024
Department of Industrial and Materials Science
Division of Material & Computational Mechanics
Chalmers University of Technology
SE-412 96 Gothenburg
Telephone +46 31 772 1000

Cover: Single sleeper tamping bank along with railway section consisting of ballast bed and three sleepers.

Typeset in LaTeX
Printed by Chalmers Reproservice
Gothenburg, Sweden 2024

Numerical analysis of railway ballast tamping using a DEM-MBD co-simulation framework

Pontus Malmsköld
Department of Industrial and Materials Science
Chalmers University of Technology

Abstract

Railway ballast tamping is a process through which geometrical defects of railways are corrected by moving the sleepers to their correct positions and inserting vibrating tamping tines into the ballast bed. The tines compact the ballast underneath the sleeper, thus ensuring proper load transfer between the sleeper and the sub-ballast. This thesis presents a DEM-MBD co-simulation framework to model the tamping procedure, and explores the differences between a conventional tamping machine, where the vibrations are generated through an eccentric shaft, and a novel fully hydraulic tamping machine, where the vibrations are generated through hydraulics. The ballast bed is modeled through the Discrete Element Method (DEM) solver Demify®, developed in-house at FCC, and the tamping machine is modeled through a Multibody Dynamic (MBD) package called Simscape Multibody found in Simulink. Furthermore, a parameter study of different tamping design parameters is performed. The fully hydraulic tamping model is validated against real-world data, showing that the model lies within the expected distribution of real-world tamping operations. The results of the simulations show that the fully hydraulic tamping model is able to compact the ballast bed to a higher degree while maintaining lower forces acting upon the ballast particles as compared to the conventional tamping model. The parameter study reveals that the vibrational amplitude significantly affects the results of the tamping process, both for the conventional and for the fully hydraulic tamping model. Different vibrational frequencies affect the fully hydraulic tamping model significantly, while it only has some minor effects on the conventional tamping model.

Keywords: Railway ballast tamping, Discrete element method, Multibody dynamics, Fully hydraulic tamping machine, DEM-MBD co-simulation, Functional mockup interface.

Acknowledgements

I would like to extend my thanks to my supervisor Johannes Quist for providing a thorough insight into the Discrete Element Method and its many applications. You have continuously provided a good source of discussion regarding all the different facets of the thesis, from modeling to report writing and evaluation of results. I would also like to express my appreciation to my supervisor Anita Ullrich who has given a significant amount of help when it comes to modeling, coding and report writing, while simultaneously always providing helpful discussions. Further, I want to thank the DEM team at FCC for providing support. I look forward to continue working together with you in the future. I want to thank my examiner Fredrik Larsson who has provided interesting discussions and valuable feedback through the course of the project.

I want to express thanks to Roland Bång of Infranord for providing highly valuable insights into railway ballast tamping. I would also like to express my gratitude to Bernhard Lichtberger of System7 for giving insight into the fully hydraulic tamping machine.

Finally, I would like to give special thanks to my family and friends who have supported me through not just this project, but through five whole years of studies. I want to thank Caroline for your continuous support along with your feedback on the report.

This work has been supported in part by the InfraSweden2030 program funded by the Swedish Governmental Agency for Innovation Systems, VINNOVA.

Pontus Malmsköld, Gothenburg, June 2024

List of Acronyms

Below is the list of acronyms that have been used throughout this thesis listed in alphabetical order:

DEM	Discrete Element Method
MBD	Multibody Dynamics
FMI	Functional Mockup Interface
FMU	Functional Mockup Unit
GPU	Graphics Processing Unit
FCC	Fraunhofer-Chalmers Center
API	Application Programming Interface
ODE	Ordinary Differential Equation
HMD	Hertz-Mindlin-Deresiewicz
DOF	Degree of Freedom
PI	Proportional Integral
CDF	Cumulative Distribution Function

Nomenclature

Below is the nomenclature of parameters and variables that have been used throughout this thesis.

Parameters

m	Mass $[kg]$
ρ	Density $[kg/m^3]$
E	Young's modulus $[GPa]$
ν	Poisson's ratio [-]
μ	Frictional coefficient [-]
e	Coefficient of restitution [-]
G	Shear modulus $[Pa]$
R	Particle radius $[m]$

Variables

$\mathbf{v}_i$	Velocity $[m/s]$
ω_i	Rotational velocity $[rad/s]$
$\mathbf{F}_i^g$	Gravitational force $[N]$
$\mathbf{F}_{ij}^c$	Contact force $[N]$
$\mathbf{M}_{ij}$	Contact torque $[Nm]$
$\mathbf{I}_i$	Moment of inertia kgm^2
t	Time $[s]$
dt_R	Rayleigh time step $[s]$
dt	Time step $[s]$
F_{norm}	Norm of forces $[N]$
ξ_{cyl}	Cylinder damping coefficient $[N/ms]$

n_{std}	Number of standard deviations from mean [-]
$n_{std,f}$	Number of standard deviations from mean for compaction force [-]
$n_{std,sp}$	Number of standard deviations from mean for squeeze path [-]
$n_{std,norm}$	Norm of $n_{std,f}$ and $n_{std,sp}$ [-]
pd_c	Packing density criterion [-]

Contents

List of Figures

List of Tables

1
Introduction

1.1 Motivation

On an average day in 2022, the Swedish railway network transported 420 000 people and goods with a total weight of 230 000 tonnes daily [1] across roughly 15 600 km of tracks [2], which shows the important role of the railway system in Sweden. Maintaining smooth operations of this highly complex system is therefore of vital importance.

A key factor in ensuring the functional capabilities of the railway system is maintenance. The railway system is continuously subjected to wear through traffic and weather. One area that is highly exposed to wear is the ballast bed, which is a key structural component of ballasted railway tracks. An illustration of a ballasted railway track is seen in Figure 1.1. The ballast bed consists of crushed stone particles, upon which the sleepers rest. A sleeper is a slab, typically made of concrete, upon which the rails are fastened. The main function of the sleeper and ballast bed is to maintain a constant position of the rails and to transfer the load of the traffic into the layers below the ballast.

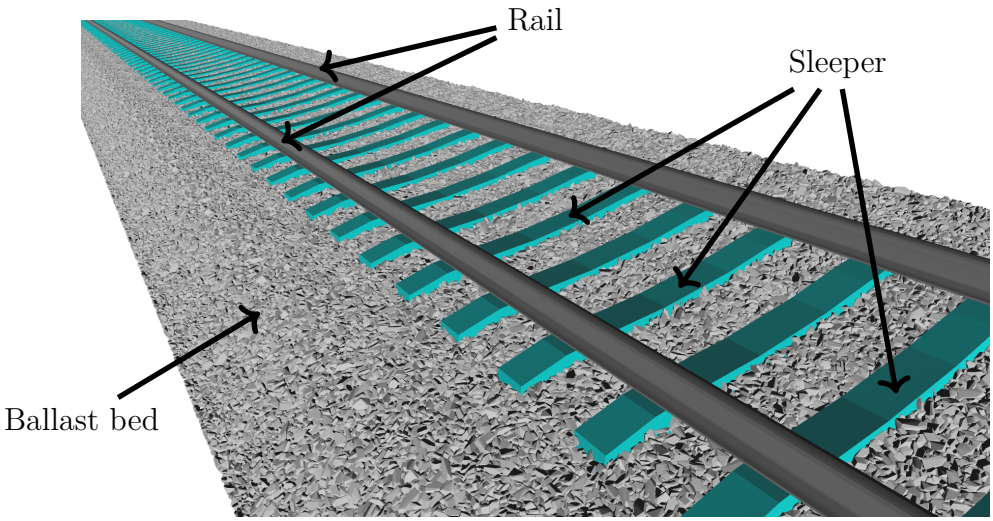

Figure 1.1: Illustration of railway track with key features highlighted.

Due to the large dynamic forces from heavy traffic, some geometrical defects of the rails, such as settlements, occur over time. These geometrical defects of the sleepers

and rails pose a significant problem for railway traffic, they can lead to accidents such as derailments, uncomfortable rides and create unfavorable interactions between the train wheels and the rail [3]. These defects may be corrected through a process called tamping.

Through tamping, geometrical defects of the rail may be corrected by lifting the sleepers and compacting the ballast underneath the sleeper. Firstly, the geometry of the track is measured, from which the displacement of each sleeper is calculated, after which the sleeper being tamped is lifted to its correct position [4]. Several tools, called tamping tines, are then inserted into the ballast bed on either side of the sleeper and compacts the ballast beneath the sleeper. The compacted ballast forms a load bearing base for the sleeper. The tamping process is performed by a tamping machine, as seen in Figure 1.2. Different models of tamping machines may tamp one or more sleepers during a tamping cycle.

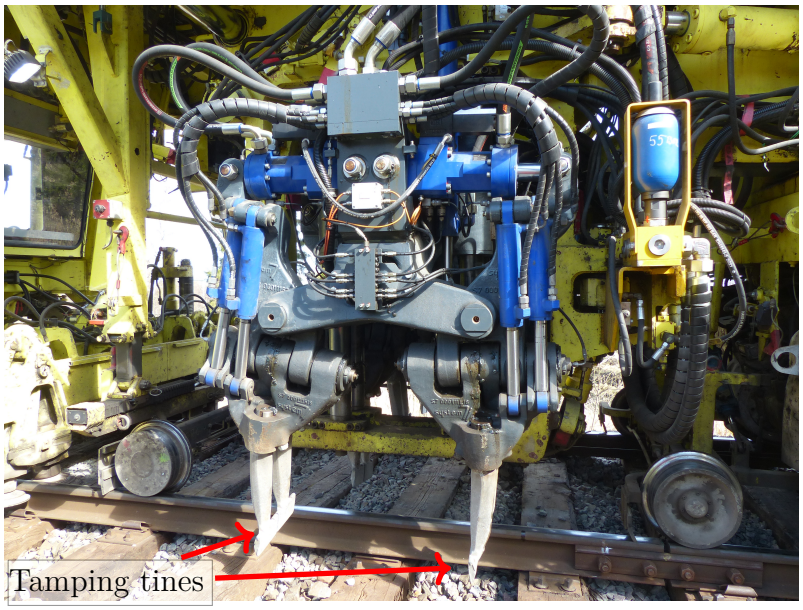

Figure 1.2: Tamping machine.

The tamping process causes heavy wear of the ballast bed through particle breakage and abrasion [5]. This degradation of the ballast bed lowers its load bearing capabilities, and causes geometrical defects to occur at an increased rate. For this reason, a minimally invasive tamping process is desirable to minimize the rate of degradation of the ballast bed.

In order to lower the shear resistance of the ballast bed, and in turn significantly lower the compaction force required of the tamping tines, vibrations of the tamping tines are induced [6]. The conventional form of tamping, which induces vibrations through an eccentric shaft connected to the hydraulic cylinder, has been used for over 70 years [7]. A newer type of tamping utilizes hydraulics instead to induce the vibrations. This hydraulic method affords a higher level of control in terms of varying amplitude and frequency of the vibrations.

Comparing the conventional and fully hydraulic methods in terms of the effects they have on the condition of the ballast bed is the main focus of this thesis. Due to the large scale, high cost and difficulty of constructing and quantifying the results for a real-world experiment, the tamping process is studied using numerical simulations.

The ballast bed is simulated using the Discrete Element Method (DEM) [8]. DEM is the dominant numerical method for modeling large particle systems. In this method, individual particles as well as all applied forces are tracked in a Lagrangian framework. Through the applied forces, the trajectory and rotation of each particle can be calculated for a set time step. The tamping machine is simulated with Multibody Dynamics (MBD). MBD is a numerical method for simulating dynamic systems of rigid bodies connected via various joints. These two numerical methods are solved using different software. In order to model both domains in a coupled simulation, a co-simulation framework called Functional Mockup Interface (FMI) is applied, through which the two solvers are coupled.

The master thesis project is performed within the **Vinnova InfraSweden2030 DigiRail** project. The work carried out within this thesis is of great interest to Infranord, one of the partners of the **DigiRail** project, who is interested in evaluating the differences between conventional and fully hydraulic tamping machines. Infranord currently owns several conventional tamping machines and one fully hydraulic tamping machine, produced by System7, through which data for validation had been provided for this thesis.

1.2 Literature Review

For modeling of the tamping process, DEM is capable of providing critical insight into the tamping process. In this section, further insight is given with regards to previous advances made in modeling the tamping process with DEM.

Zhou et al. [9] simulate a small section of the ballast bed using a multisphere model for the ballast particles. Employing a multisphere model in order to represent complex particle shapes have long been the norm due to the ease of handling numerical calculations for multisphere models. Only a small section of the sleeper is included in the domain, which restricts the simulation to the use of only two tamping tines for a single-sleeper tamping machine. A similar setup is done by Wang et al. [10], however with a two-sleeper tamping machine yielding four tamping tines. Both of these simulations control the tamping arms through rigid motions.

Simulating the tamping machine through MBD is done by Shi et al. [11] using a DEM-MBD co-simulation. A complete section of the ballast bed with four sleepers is simulated using a multisphere model. The MBD model used is restricted to not include the hydraulic cylinders and eccentric shaft, the effects of these are instead applied through fixed rotations of the tamping arms around fixed pivot points. Further developments of the model are made by Shi et al. shows the impact of includ-

ing a particle breakage model [12] and the impact of different penetration depths [5].

Zhang et al. [13] utilize a polyhedral particle model for the ballast bed, and use DEM-MBD coupling to simulate both the ballast bed and the tamping machine. The hydraulics of the tamping machine are not included, and as such the compressive movement and vibrations are applied through rotations of the tamping arms.

There exists a research gap in the MBD models used for DEM-MBD coupling simulations for tamping where the movements of the tamping arms and tines have not been simulated with a model that includes hydraulics. As a consequence of this, the different effects of conventional and fully hydraulic tamping methods have not been investigated.

Table 1.1 collects studies on DEM tamping. *Sleepers* refers to the number of sleepers that is tamped by the modeled tamping machine.

Table 1.1: Literature review of numerical simulations of tamping.

Reference	Year	MBD	Vibrations	Particle Model	Sleepers
Zhang et al. [13]	2023	Yes	Sinusoidal	Polyhedron	3
Chi et al. [14]	2023	Yes	Sinusoidal	Multisphere	1
Shi et al. [5]	2022	Yes	Sinusoidal	Multisphere	2
Zhou et al. [9]	2013	No	Sinusoidal	Multisphere	1
Wang et al. [10]	2012	No	Sinusoidal	Multisphere	2

1.3 Scope & Research Questions

The objective of the project is to investigate how different tamping methods influence the probability of ballast fracture and degradation as a consequence of the interaction between the tamping tool and particle assembly. There are two different tamping methods that are evaluated, conventional tamping, where vibrations are generated through rotation of an eccentric shaft, and a fully hydraulic method, where vibrations are generated solely through hydraulics. Four research questions are stated below, which aid in dividing the previously stated objective into smaller parts, with quantifiable results.

1. How may the two tamping processes be modeled in a DEM-MBD co-simulation framework?
2. How may the results of the tamping process be quantified in a manner that properly exploits the strengths found in a DEM-MBD co-simulation as compared to real-world experiments?
3. In what way do the two tamping processes vary in terms of the previously mentioned quantifiable results?
4. In what way do the results of the tamping process change with varying values of critical tamping design parameters?

The two tamping methods are simulated with the same setup, and the results from these simulations are compared.

1.4 Software

All DEM simulations seen in this thesis are simulated with the DEM solver Demify®. Demify® is a high performance computing DEM solver with GPU parallelization capabilities, developed at the Fraunhofer-Chalmers Center (FCC). The solver is written in C++ and is for the purpose of this thesis accessed through a Python API [15].

Further, all MBD simulations in this thesis are solved through Simscape Multibody, which is accessed through the Matlab Simulink environment [16]. Simulink is a graphical programming environment for simulation of dynamic systems. Simulink may be expanded with Simscape, which provides access to tools for modeling a variety of different physical systems. In this thesis, the Simscape libraries used are Multibody dynamics, through which the moving parts of the tamping machines are modeled, and Fluids, through which hydraulics are modeled. Moreover, the Simulink foundation library is utilized for more general control modeling, such as amplitude control or signal generation.

These two simulations are coupled by a co-simulation framework called Functional Mockup Interface (FMI) [17]. Through FMI, one of the simulations, called the slave, is compiled into a Functional Mockup Unit (FMU), through which the slave simulation is run with a number of specified inputs and outputs. The FMU is then imported into the so-called master simulation, through which the inputs and outputs of the FMU act as the coupling between the two simulations.

For this thesis, the FMU is complied using the Python library *pyfmu* [18]. Demify® acts as the slave simulation, and Simulink as the master simulation.

1.5 Outline

In Chapter 2, the theoretical background related to the tamping process and the different numerical methods are presented. The modeling process of the problem is presented in Chapter 3, and the verification of the models are seen in Chapter 4. Chapter 5 contains the results from simulating the previously described models along with analysis of said results. These results are further discussed in Chapter 6 and conclusions based on the results are drawn.

2
Background

2.1 Railway Ballast Tamping

The structure of the railway track and the tamping machines studied in this thesis are presented and explained in this chapter. The railway track composition is explained first in Subsection 2.1.1, which gives a background into what function the different parts of the railway track plays. Composition and wearing of the ballast bed are also discussed in this section. Next, the tamping process is presented thoroughly in Subsection 2.1.2, after which critical design parameters of a tamping machine are presented in Subsection 2.1.3. Differences and similarities between the two types of tamping machines are discussed in Subsection 2.1.4. Lastly, the issue of quantifying the effectiveness of the tamping process is presented in Subsection 2.1.5.

2.1.1 Railway Track Composition

The railway track consists of several different parts, as shown in Figure 2.1. The cross section is based on a typical railway track consisting of subsoil, subballast, ballast, sleeper and rails.

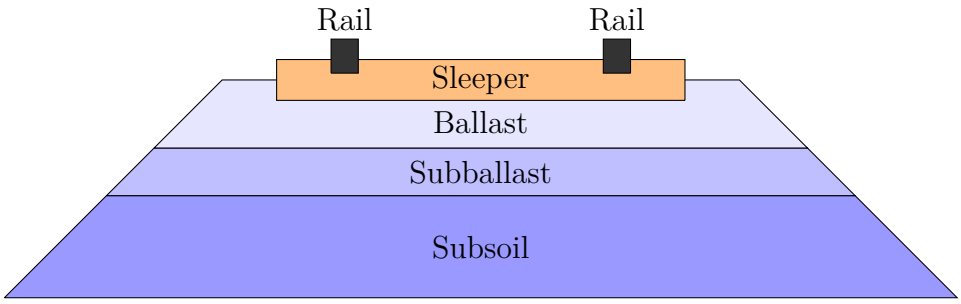

Figure 2.1: Cross section of railway track, modified from [19].

The ballast bed and the sleeper are the parts of the railway track that interact with the tamping machine. Therefore, the scope of this project is limited to simulating these parts. The tamping machine also interacts with the rail in the lifting of the rails and sleepers, however, this may easily be modeled through translation of the sleeper. The rails are thus not included in the models. The subballast and below may be simulated using the finite element method (FEM), however, this falls outside of the scope of this project. The subballast and below are treated as a solid floor in

this project. The most important functions of the ballast bed are to evenly transfer the load from the sleepers to the subballast, to keep the displacement of the sleepers to a minimum and to facilitate drainage [4]. The shape and size distribution of the ballast particles are important factors in the ballast bed's ability to properly perform the previously stated functions. The ballast particles should have highly irregular surfaces to facilitate interlocking mechanisms between particles [6]. Smooth particles and contamination of the ballast bed impede the interlocking mechanisms between particles, thus decreasing the load bearing capabilities of the ballast bed. When a railway track is built or repaired, new ballast particles are used, which have to meet certain requirements in order to facilitate optimal interactions between the sleepers and the ballast bed.

When the railway track is newly built, the ballast bed performs the functions stated in the above paragraph optimally. As the ballast bed is exposed to large dynamic loads from traffic, the ballast particles are worn, which causes a degradation of the ballast bed. Over time, smaller, wedge shaped fragments are broken off from the ballast particles. Initially, these fragments improve the resistance to shearing in the ballast bed. However, as more traffic passes over the ballast bed, the ballast particles and fragments are crushed into finer particles, which encloses the ballast particles and lowers the load bearing capabilities and shearing resistance of the ballast bed [4]. The fine particles also hinder drainage of the ballast. The three stages can be seen in Figure 2.2. The tamping process may have significant adverse effects on the ballast bed performance through wear of the ballast particles. This is further discussed in the coming section.

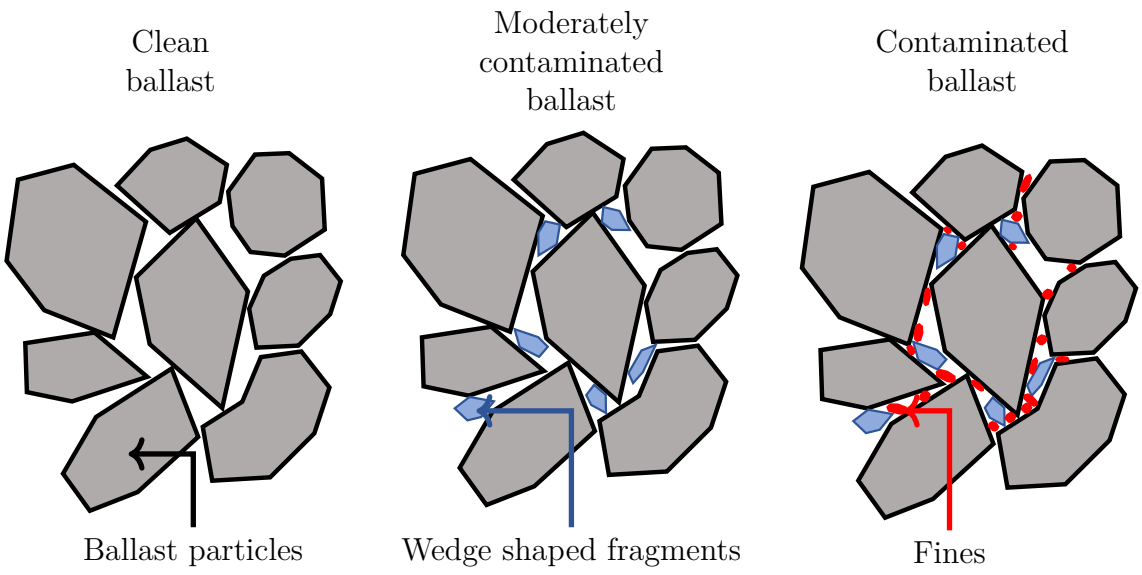

Figure 2.2: Contamination degree of ballast bed, modified from [4].

2.1.2 Tamping

Tamping is a process in which the sleeper is moved to its proper position, and the ballast underneath the sleeper is compacted to ensure proper load transfer from sleeper to subballast. Before tamping, the geometry of the rails is measured and the target track position is calculated. The sleeper being tamped is lifted to its correct position right before the tamping cycle begins. The part of the tamping machine that performs the tamping operation is called a tamping bank, an illustration of which can be seen in Figure 2.3. The tamping bank consists of 8 tamping arms which can be rotated around a pivot point. The pivot points around which the tamping arms are rotated can also be seen in Figure 2.3.

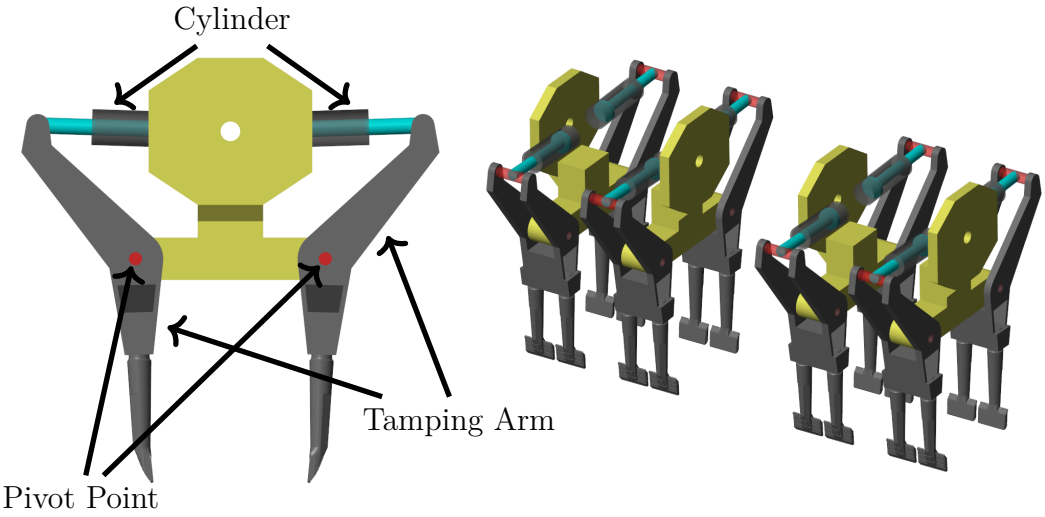

Figure 2.3: Illustration of a tamping bank.

At the bottom of the tamping arms, several tamping tines are fastened. The tamping tines are the tools that interact with the ballast bed. Two examples of tamping tines are shown in Figure 2.4. Vibrations of the tamping tines are induced, typically through an eccentric shaft connected to the hydraulic cylinders, however, this may also be done through hydraulics.

Figure 2.4: Two tamping tines, one with significant wear (top) and one with less wear (bottom).

In order to perform the compaction of the ballast, the tamping bank is moved downwards which causes the tamping tines to penetrate the ballast bed. The tines are penetrated until a certain depth is reached, called the penetration depth. When the proper penetration depth is reached, the pistons move outwards, which causes rotation around the pivot point. This rotation causes the tamping tines to move towards the sleeper, thus compacting the ballast bed by applying a compressive force to the ballast. This compaction is done either for a specified time, or until some criterion has been reached. This criterion is further explained in Subsection 2.1.4. After the compaction is done, the tamping tines are removed from the ballast bed by retracting the pistons while moving the tamping bank upwards.

The vibrations of the tamping tines serve several important functions: to lower the shear resistance of the ballast bed, thus lowering the force needed for compaction, and to rearrange the particles being compacted to facilitate a uniform compaction. Typically, the tamping tines are vibrated with a frequency of 35 Hz and an amplitude of 4-5 mm [20].

An issue with the tamping process is the high forces involved in the procedure, often leading to ballast particle breakage [5]. The interaction of the vibrating tamping tines with the ballast particles further contaminates the ballast bed through abrasion. For these reasons, the ballast bed condition is usually degraded by the tamping process. This degradation of the ballast bed condition reduces the ability of the ballast bed to resist displacement of the sleeper, which causes settlements and other geometrical defects to occur at an increased rate. As the condition of the ballast bed gets progressively worse, it eventually needs to be replaced with fresh ballast. It is therefore of great interest to design the tamping method in such a way that the degradation of the ballast bed from tamping is minimized. This could potentially be achieved by either improving the effectiveness of the tamping procedure, thereby increasing the time until a new tamping operation needs to be performed, or by reducing the degradation of the ballast bed caused by a single tamping operation.

2.1.3 Design Parameters

Guo et al. [3] describe several parameters, which collectively describe the entire tamping process. The parameters along with a short description of each parameter are given below.

1. **Vibrational frequency**, the frequency of the tamping tine.
2. **Vibrational amplitude**, the amplitude of the tamping tine.
3. **Compaction pressure**, the static input pressure of the hydraulic cylinder used for compaction.
4. **Compaction time**, the total time of the squeezing motion.
5. **Lifting height**, the height that the track is lifted prior to tamping. Varies based on the geometrical defects of the track.
6. **Penetration depth**, the depth that the tamping tines are penetrated into the ballast bed. Defined as the vertical distance between the lower edge of the sleeper and the upper edge of the tamping tine plate.
7. **Penetration speed**, the speed at which the tamping tines are penetrated into the ballast bed.
8. **Retraction speed**, the speed at which the tamping tines are retracted from the ballast bed.
9. **Compaction times**, the number of times that the compaction operation is performed.

2.1.4 Tamping Approaches

For a conventional tamping machine, the vibrations of the tamping tines are induced by an eccentric shaft connected to the hydraulic cylinders. The amplitude of the vibrations are set by the eccentric distance and the frequency by the rotational speed of the shaft. This solution has been widely used for over 70 years [7] and affords little in terms of control during the tamping process. A new approach to tamping is to induce the vibrations through the hydraulic cylinder instead, thereby circumventing the need for an eccentric shaft and lowering the amount of moving and wear prone parts. This approach yields a higher level of control, for example, the amplitude and frequency can be changed during tamping, or the vibrations can be completely turned off on retraction [21].

Typically, the compaction time is set to a constant value, often decided by experience of the machine designer and the machine operator. Some newer machines instead utilize some compaction criterion to find the optimum compaction time on a sleeper by sleeper basis. Doing this could yield a better result by never under- nor over-tamping, thus leading to less wear of the ballast bed and a lower rate of settlements after the tamping procedure is done. One such approach is described by Lichtberger [21] where the compaction force is continually monitored by the tamping machine. During the compaction, the compressive force applied by the tamping tines typically increases as the tamping tines move closer to the sleeper. However, at a certain point, the compressive force stops increasing while the tines keep moving. This point is stated to be the optimum compaction point, and compaction should stop once this point has been reached.

2.1.5 Quantifying Tamping Effectiveness

The tamping operation is a highly complex procedure for which the results are not easily defined. The main function of the tamping operation is to correct geometrical defects of the sleeper and ensure that the rate at which new geometrical defects occur is kept as low as possible. Since these defects occur over a long time period, typically months or years through heavy cyclical load from traffic, it is difficult to investigate these defects for a numerical simulation due to the heavy computational cost of simulating even a few seconds of time. Therefore, the effectiveness of the tamping operation must be quantified in some other manner.

As previously discussed, wearing of the ballast particles plays a significant role in the rate of degradation of the ballast bed. In order to limit the rate of degradation, the wear of the ballast particles should be kept to a minimum. Investigating how the tamping process affects the wearing of the ballast particles is a computationally easier task as compared to investigating the geometrical defects over time due to the need of only simulating one tamping cycle. In this way, the wearing of the ballast particles and bed can be calculated, which gives an indication as to how rapidly geometrical defects would occur under normal traffic loads.

Several different approaches may be applied to quantify the wear of the particles during the tamping process. Particle breakage constitutes a large portion of the degradation of the ballast bed from tamping. As such, looking at the maximum force experienced by each particle gives an indication as to how likely particle breakage is. Implementation of a numerical particle breakage model would be interesting, however, it falls outside of the scope of this thesis, and as such, particle breakage is assumed to be related to the maximum force experienced by each particle.

The effectiveness of the tamping process can also be quantified by investigating if a highly compacted base has been formed beneath the sleeper with a good ability to transfer loads from the sleeper to the subballast. In this project, this is quantified through two methods: by calculating the packing density underneath the sleeper and by investigating the forces acting on the sleeper during tamping. The packing density refers to the percentage of a volume filled with particles, as opposed to void. A higher packing density suggests a higher compaction of the ballast bed. The force experienced by the sleeper gives an indication as to how many particles are in contact with the sleeper. The sleeper being in contact with as many ballast particles as possible is important in order to ensure that the ballast bed can properly transfer the loads from the sleeper to the subballast.

2.2 Numerical Modeling

Examining the tamping process by employing real life experiments is time consuming and expensive. Instead of large scale experiments, numerical modeling may be utilized to simulate the system of interest. For the tamping process, it is mainly the dynamics of the tamping machine, and the ballast-ballast, ballast-sleeper and

ballast-tamping tine interactions that are of interest. This section describes the numerical models used to simulate these dynamics and interactions. The Discrete Element Method (DEM) is described in Subsection 2.2.1, then Multibody Dynamics (MBD) in Subsection 2.2.2. Lastly, in Subsection 2.2.3, the Functional Mockup Interface (FMI) which couples the two simulations is described.

2.2.1 Discrete Element Model - DEM

The Discrete Element Method (DEM) [8] is a numerical method for simulating large particle systems. Each separate particle is represented as one discrete particle with several accompanying variables such as position, rotation, geometry, center of mass and density. These variables are tracked at the center of mass of the particle. Forces applied to the particles are calculated and tracked. By discretizing the temporal dimension, the velocity and the position of each particle can be calculated by integrating the following ODEs for a set time step [22]

$$m_i \frac{d\mathbf{v}_i}{dt} = \sum_j \mathbf{F}_{ij}^c + \mathbf{F}_i^g \tag{2.1}$$

$$\mathbf{I}_i \frac{d\omega_i}{dt} = \sum_j \mathbf{M}_{ij} \tag{2.2}$$

Here, $\mathbf{v}_i$ is the velocity and ω_i is the rotational velocity of particle i, while m_i and $\mathbf{I}_i$ are the mass and moment of inertia of the particle. $\mathbf{F}_i^g$ is the gravitational force applied to particle i. $\mathbf{F}_{ij}^c$ and $\mathbf{M}_{ij}$ are the force and the torque applied to particle i given by collision of particle i and j. A particle in a collision is affected by both an interaction force and an interaction torque of the same magnitude with opposite signs as the other particle in the collision. Additional forces may be added depending on the simulation case, such as forces from a fluid surrounding a particle or cohesive liquid bridge forces in a wet ballast bed. In this thesis, a dry ballast bed condition is considered. As such, no other forces are of interest and are therefore not included.

Collisions between particles are an important factor in DEM simulations. For a ballast bed, the packing density is high [23], this means that each particle is in contact with several other particles at all times, leading to a large number of collisions to solve for simulations of a ballast bed. One way of solving collisions is to employ a *soft sphere* contact force model. A *hard sphere* model may also be used, however, this model is more applicable for dilute systems with a lower packing density. For a system with a high packing density, a *soft sphere* model is preferable [24], and is thus used in all DEM simulations done in this project.

For a *soft sphere* model, a sufficiently small time step is chosen such that particle-particle interactions can be seen as a small overlap in volumes, from which the forces applied on the particles from the collisions can be modeled. An example of such a force model is Hertz-Mindlin-Deresiewicz (HMD) [25]. Through HMD, the overlap between the particles is modeled as a simple spring-damper system. The HMD contact force model is illustrated in Figure 2.5, where normal contact forces between

the particles are represented by a spring and a damper, and the tangential forces are represented by a spring, a damper and a frictional element.

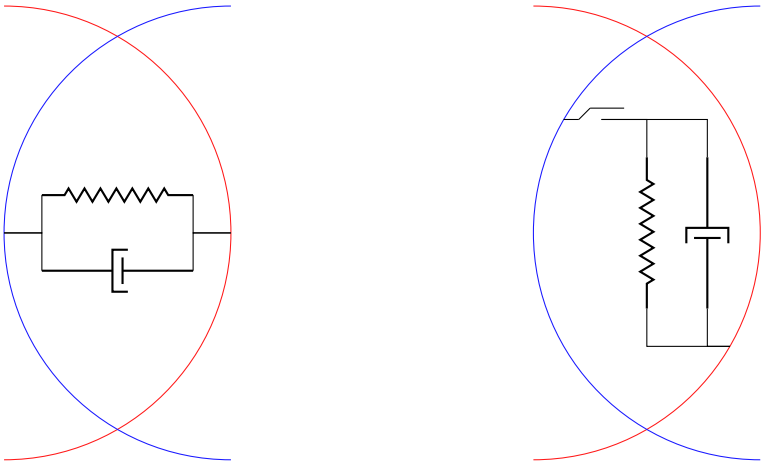

Figure 2.5: Illustration of the HMD model for overlapping particles with normal forces (left) and tangential forces (right).

The HMD model is made for spherical particles, where the forces are based on the overlap between the spheres. This overlap is easy to calculate from the particles center of mass and radius. This model needs to be expanded in order to work with non-spherical particles. For this project, dilated polyhedrons are used to represent the complex geometry found in ballast particles. In a dilated polyhedron, a Minkowski sum between a convex triangulation and a sphere is defined [26]. This can be seen as a sphere being swept across the surface of a polyhedron. Through the dilation, the HMD model can easily be employed for complex particles by using the radius of the sphere being swept across the polyhedron to calculate the overlap between particles. A few restrictions of this model are that the polyhedron must be convex, and that the overlap between particles cannot exceed the dilation radius (the radius of the sphere being swept across the polyhedron). If the overlap exceeds the dilation radius, the HMD model is undefined. A visual representation of a dilated polyhedron can be seen in Figure 2.6.

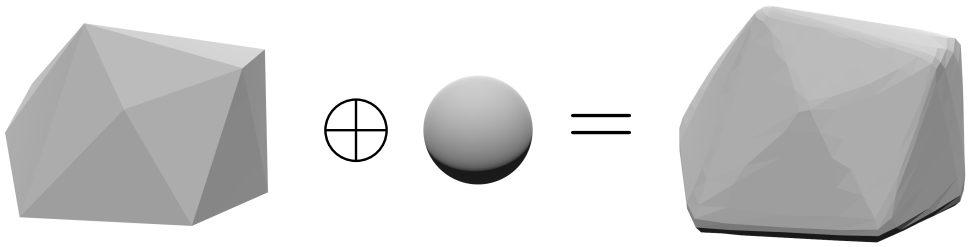

Figure 2.6: Minkowski sum between a rectangle and a circle.

Computational performance is an important aspect of DEM simulations due to the often large number of particles and small time steps. The DEM simulations in this

project are therefore performed on the GPU through Demify®, which allows for efficient simulations due to parallelization.

2.2.2 Multibody Dynamics - MBD

Multibody Dynamics is a numerical method used for simulations of dynamic systems of rigid bodies. This method may sound similar to DEM, however, MBD does not handle collisions between particles. Instead, the main goal of an MBD model is to simulate the interactions of rigid objects connected to each other via joints. These joints allow for different kinds of relative movement between bodies. In total, there are 6 degrees of freedom (DOF) for a rigid object to move in, three translational and three rotational DOFs. Joints typically fix a number of DOFs while keeping the remaining DOFs free. A few examples of these joints are: fixed joint (all DOFs fixed), prismatic joint (one translational DOF free, remaining DOFs fixed), revolute joint (one rotational DOF free, remaining DOFs fixed) and cylindrical joint (one translational and one rotational DOF free, remaining DOFs fixed).

Forces and torques can be applied to rigid bodies to induce movement. The forces and torques of interest in this project are body forces, such as gravity, and externally applied forces or torques. These externally applied forces are retrieved from some other domain than MBD, such as hydraulics or DEM.

Once all bodies are connected through joints and forces and torques are applied, the ODEs which describe the dynamic system are solved for discrete time steps. As previously mentioned in Section 1.4, all MBD simulations are performed through Simscape Multibody in Simulink.

2.2.3 Co-Simulation Framework

As previously stated, the two numerical simulations are coupled by a co-simulation and model exchange framework called Functional Mockup Interface (FMI). For this project, FMI is used for co-simulations. The main difference between co-simulation and model exchange is that for co-simulations there are two separate simulations, each with its own solver, which are then coupled [17]. For model exchange, only one solver is needed for the simulation, and an external model is imported into the simulation via FMI.

In the co-simulation framework, the two simulations are able to communicate via discrete communication points, through predefined inputs and outputs. One of the simulations, called the master simulation, controls the data exchange between the simulations. In between the communication points, the simulations are solved independently from each other, though in a synchronized manner. For example by solving for an equally long time in between communication points. This synchronization is handled by the master simulation. The simulation being controlled by the master simulation is called the slave simulation.

In order to utilize the slave simulation, it has to be compiled into a Functional Mockup Unit (FMU). The FMU is a zip file with the extension *.fmu*. In this file, all relevant information regarding the slave simulation is stored, including input and output variables from the FMU. The FMU file is then imported into the master simulation and controlled from there.

3
Modeling

This section shows the process of modeling the ballast bed, the tamping machines and the coupling of the two. All modeling choices and assumptions made are presented here and explained. First, the modeling of the ballast bed through DEM is shown in Section 3.1, after which the modeling of the tamping machine by utilizing MBD is presented in Section 3.2. Next, the coupling between the two simulations is explored in Section 3.3. Finally, simulation parameters and the parameter study procedure are given in Section 3.4 and Section 3.5 respectively.

3.1 Discrete Element Method

As discussed previously, the ballast bed is modeled with the DEM software Demify®, through which the governing equations found in Subsection 2.2.1 are solved. The tamping simulation is run a multitude of times, for example during the validation of the model or during the parameter study, both of which are found in Chapter 5. Maintaining a low computational time is therefore of high priority. Generation of the ballast bed is generally a computationally demanding process, and as such, the ballast bed should be generated prior to the tamping simulation. This way, the state of the ballast bed after generation can be saved and imported as the initial state of the bed for simulation of the tamping process. This methodology provides a significant improvement in the computational efficiency as compared to generating a new ballast bed for each tamping simulation. Additionally, using the same initial state of the ballast bed for all tamping simulations eliminates some differences between separate simulations which helps facilitate comparison. Adversely, the statistical variation of utilizing different ballast beds cannot be evaluated.

The first step of constructing the ballast bed is to ensure that the ballast particles are modeled as particles that represent a real-world ballast bed. The main properties of a DEM particle that governs the behaviour are: particle shape, contact force model, material properties and particle size distribution.

The particle shapes are based on 3D scans of ballast particles available at FCC. These scans are of high resolution, which gives a mesh with a large number of triangles. Even though using these high resolution meshes in the simulation would give the most accurate representation of an actual ballast particle, it is not computationally feasible and the mesh therefore has to be reduced to a lower number of triangles. The high resolution mesh of a ballast particle, consisting of 100 000 triangles, can be

seen to the left in Figure 3.1. In the middle a lower resolution mesh, consisting of 60 triangles, is shown. For this project, a dilated polyhedron model is employed to represent the particles, which is explained in detail in Subsection 2.2.1. The convex hull of the mesh in the middle is calculated and show to the right in Figure 3.1. Of these meshes, the low-resolution convex mesh is used for the simulations. Six different particle meshes, which have a lower resolution and whose convex hull is computed, are employed for the ballast bed.

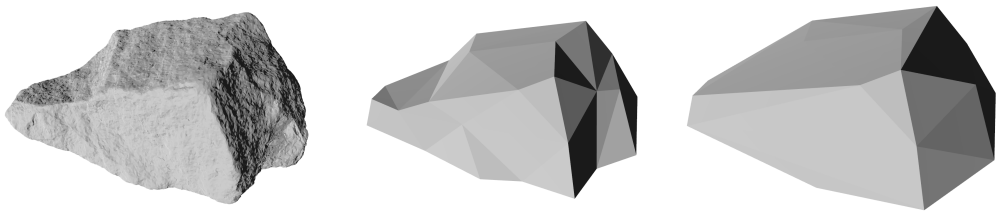

Figure 3.1: Different meshes of ballast particles.

The same material parameters are applied to all ballast particles in the model. These can be seen along with the values applied in the simulations in Table 3.1. The given values have been shown to work well in previous **DigiRail** projects. Additional work could be carried out with regards to calibration of the parameters, however, it falls outside of the scope of this project. Material parameters for rigid objects can also be seen in the table. These rigid objects are either made of steel or concrete. The tamping tines and arms are made of steel while the domain walls and floor along with the sleepers are made of concrete.

Table 3.1: Material parameters for ballast particles

Type	Property	Symbol	Value	Unit
Ballast material	Density	ρ	2700	$\frac{kg}{m^3}$
Ballast material	Young's modulus	E	1	GPa
Ballast material	Poisson's ration	ν	0.27	-
Rigid object material, concrete	Density	ρ	3000	$\frac{kg}{m^3}$
Rigid object material, concrete	Young's modulus	E	10	GPa
Rigid object material, concrete	Poisson's ration	ν	0.3	-
Rigid object material, steel	Density	ρ	7800	$\frac{kg}{m^3}$
Rigid object material, steel	Young's modulus	E	210	GPa
Rigid object material, steel	Poisson's ration	ν	0.3	-
Particle-Particle interaction	Friction	μ	0.6	-
Particle-Particle interaction	Coefficient of restitution	e	0.2	-
Particle-Rigid object interaction	Friction	μ	0.6	-
Particle-Rigid object interaction	Coefficient of restitution	e	0.2	-

The coefficient of restitution described in the table refers to the ratio between the particle velocity after the collision and the particle velocity before the collision.

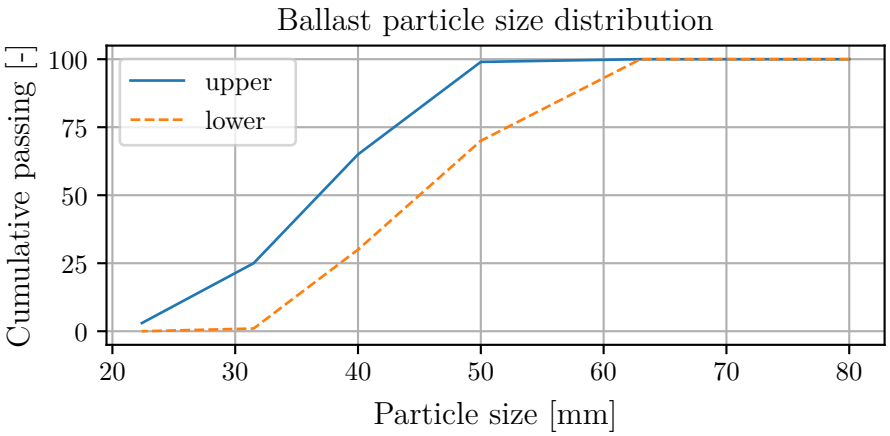

Figure 3.2: Ballast particle size distribution with upper and lower limit.

When generating the particles for the ballast bed, the size distribution follows category A found in the Swedish standard SS-EN 13450, Table 1 [27]. This size distribution is seen in Figure 3.2.

In order to generate the ballast bed along with sleepers, the following procedure is followed:

1. **Generate initial cell**: An enclosed space measuring $1 \times 1 \times 2$ m is created in which particles are generated at the top of the domain at a specified frequency and mass-rate, and are allowed to fall down until the particles fill up over half of the volume. At this point, the generation stops and all particles above 1 m are removed. This yields a $1 \times 1 \times 1$ m cube of ballast particles. The final state is saved as a so-called *initial cell*
2. **Fill volume**: A mesh of the outline of the volume beneath the sleepers that are to be filled with ballast particles is created. This geometry is then filled by inserting and copying the initial cell until the specified volume is filled with ballast particles.
3. **Place sleepers**: The sleepers are placed on top of the ballast bed.
4. **Generate particle rain**: Particles are generated above the sleepers and allowed to fall down, in the same way as for the initial cell, and fill the gaps in between the sleepers.
5. **Remove excess particles**: All particles above a certain point are removed, in order to avoid any particles laying on top of the sleepers and to control the level of the particles.
6. **Let bed settle**: Let the bed settle for five seconds in order to reach a steady state.

After the bed is generated, the final state is saved and then used in the tamping simulation. The computational time scales with the number of particles in the ballast bed, thus, in order to keep the computational time reasonable, only a small section of the railway track is simulated. In the directions of the rails, solid walls are placed to contain the ballast particles within the computational domain. For this project, a single sleeper tamping machine is used, for which it is chosen to use a track section consisting of three sleepers. The ballast bed therefore consists of

a section with three sleepers and ballast 0.3 m outside of the sleepers. A visual representation of the ballast bed section with sleepers can be seen in Figure 3.3.

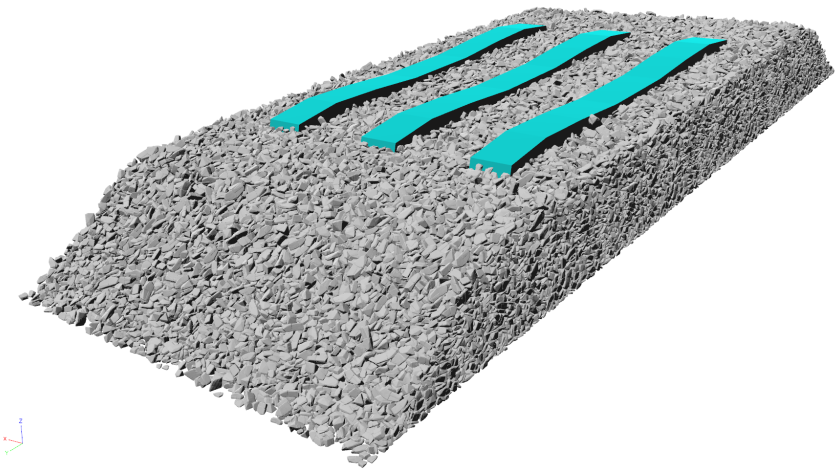

Figure 3.3: Ballast bed section with three sleepers.

The sleepers and tamping tines are defined as rigid objects and placed at origin in the initial setup for the DEM simulation. The movement of the rigid objects is done by dynamically updating the position, rotation, velocity and rotational velocity. The update of these variables are performed by the DEM-MBD coupling. This is further elaborated upon in Section 3.3.

3.2 Multibody Dynamics

The modeling of the tamping machine with MBD is presented in this section. First, the hydraulic cylinder model is shown, then the MBD model of the hydraulic tamping machine, after which modeling of the tamping sequence is discussed. Lastly, the conventional tamping model is implemented as an extension of the hydraulic tamping model.

3.2.1 Hydraulic Cylinder

The hydraulic cylinder utilizes two Simscape packages, Fluids and Multibody. These two packages contain their own individual simulation domains. The two separate domains are connected through interface and converter blocks in order to create a model where both domains are simulated. The goal of the hydraulic cylinder model is to have a model that accepts pressure as an input and translates the applied pressure to a one dimensional translational movement. The hydraulic cylinder shown here is based on the double actuating cylinder model described in [28]. Figure 3.4 shows the hydraulic cylinder model in Simulink. The piston and the cylinder, which are the two solid objects of the hydraulic cylinder, are connected through a prismatic joint, which allows for translation in one dimension. A non-zero damping coefficient ξ_{cyl} is applied to this joint to model the friction between moving parts of the tamping arm. The friction is here modeled as a single damping coefficient in the cylinder,

all other joints have a damping coefficient equal to zero. The prismatic joint is actuated through an interface between the multibody domain and a translational domain. The translational domain in turn is connected to the fluid domain through the piston chambers where a pressure is converted to a translational movement. The colours of the signal lines represent different domains. These domains and their respective colours are: Isothermal Liquid Domain (blue), Mechanical Translational Domain (green), 3-D Mechanical (Grey), Physical Signals (red) and the basic Simulink signals are given as black lines.

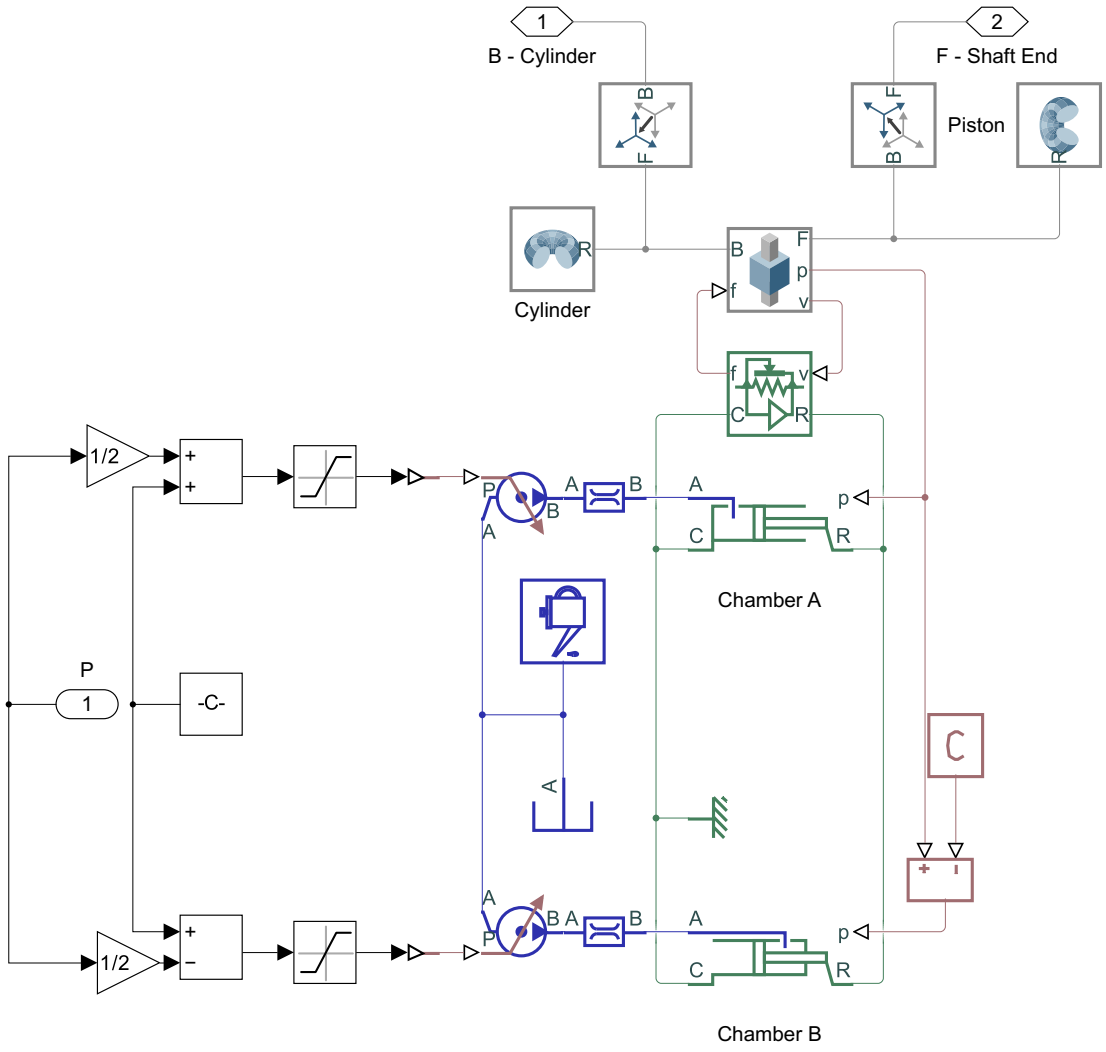

Figure 3.4: Simulink model of a hydraulic cylinder.

3.2.2 Tamping Bank

By utilizing the multibody domain together with the previously described hydraulic cylinder, the tamping bank is modeled. All eight tamping arms of the tamping bank refer to the same tamping arm model. A reference frame, which is an object in Simscape Multibody for defining relations between bodies, is utilized as the origin of the tamping bank, which in turn is used for translations of the entire tamping bank. Revolute joints (allows for rotation in one dimension) connects the cylinder and pivot point of the tamping arm to the tamping bank frame. Another revolute joint connects the end of the piston to the tamping arm. Figure 3.5 shows the modeled tamping arm along with all revolute joints.

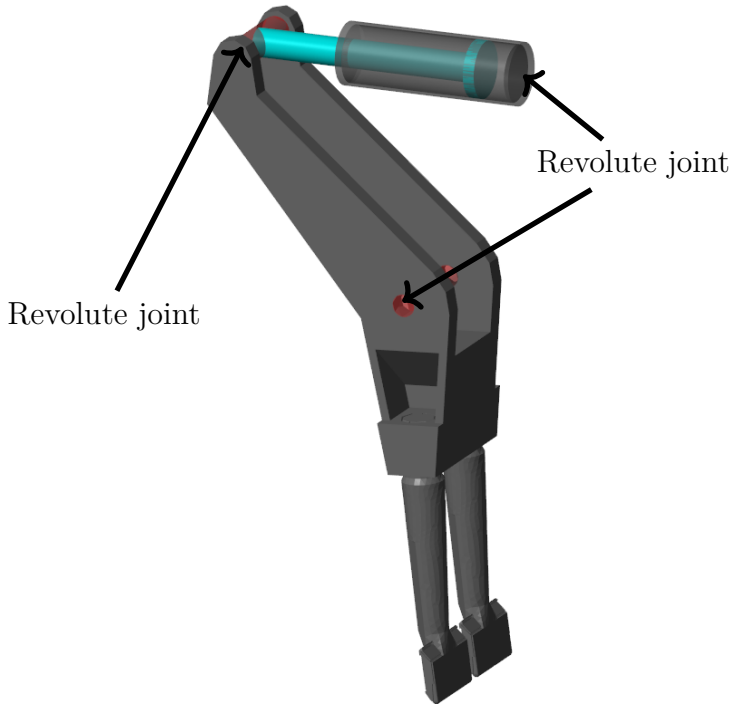

Figure 3.5: Tamping arm with revolute joints.

The revolute joints connected to the cylinder and the pivot points are set at a fixed distance from the tamping bank frame, while the revolute joint that connects the arm and cylinder is free to move. These constraints ensure that the tamping arm moves as intended. The sleeper geometry is added with reference to the global coordinate system, which allows for control of the sleeper position in Simulink. Figure 3.6 shows the full tamping bank along with sleepers and a solid representation of the ballast bed. The tamping bank consists of eight tamping arms, along with geometry that connects the tamping bank to the pivot points, this geometry is mainly added for visualization purposes.

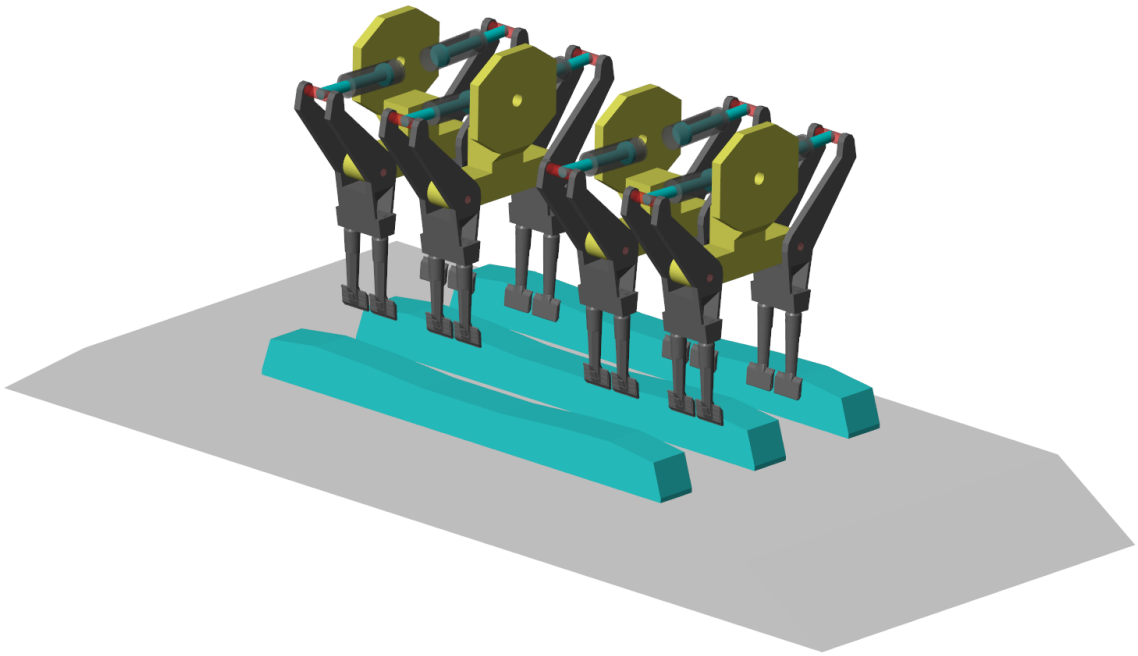

Figure 3.6: Simulink model of tamping bank.

3.2.3 Control

The tamping sequence is mainly controlled through the use of Simulink blocks. At the beginning of the simulation, the tamping bank is positioned such that the tamping tines are located just above the upper edge of the sleeper. The tamping bank is moved downwards with a constant penetration speed. The distance between the bottom of the sleeper to the top of the tamping tine plates is measured and the downward movement is stopped when the proper penetration depth is reached. When the tamping bank has stopped moving, a pressure signal is sent to the cylinders, which causes the squeezing movement to start. The compaction is performed for a set number of seconds given by the compaction time. After the compaction is performed, a negative pressure is sent to the cylinders causing the tamping tines to retract while the tamping bank is simultaneously moved upwards. When the tamping bank has reached the initial position, the simulation is stopped.

3.2.4 Fully Hydraulic Tamping

In order to further develop the fully hydraulic tamping machine, a compaction criterion for the squeezing motion and the ability to switch the vibrations on and off are implemented. Subsection 2.1.4 describes a compaction criterion where the squeezing motion is stopped when the compaction force has plateaued while the tines still move closer to the sleeper. Implementing this compaction criterion is difficult due to the high levels of noise in the data given by the simulation. It is therefore decided to implement a compaction criterion based on the packing density of the ballast bed. This choice is mainly done because of the ease of implementation and because continually measuring the packing density is easily performed in a DEM simulation,

but not possible in a real-world experiment. Using the packing density thus properly exploits the strengths found in DEM compared to real-world experiments. The packing density underneath the middle sleeper is continually measured throughout the simulation.

In order to measure the packing density, a box is created, which has the same length and width as the sleeper and has a height of 100 mm. It is placed underneath the sleeper at a depth of 100 mm. Figure 3.7 shows the evolution of the packing density underneath the middle sleeper for a compaction time of 2 s. This compaction time is significantly longer than what is typically used, however it provides insight into how the packing density changes over time. It can be seen that the initial packing density is low, this is due to no pre-compaction of the ballast bed being performed. The packing density decreases as the tines are inserted into the ballast bed, although, as the compaction is performed, the packing density is increased. The packing density stabilizes at roughly 0.655, though it stabilizes at this point after reaching a previously higher point at roughly 0.667. Therefore, both 0.655 and 0.66 are used for the compaction criterion and compared. As soon as the chosen packing density is reached, the compression is assumed to be done and the tamping tines are retracted.

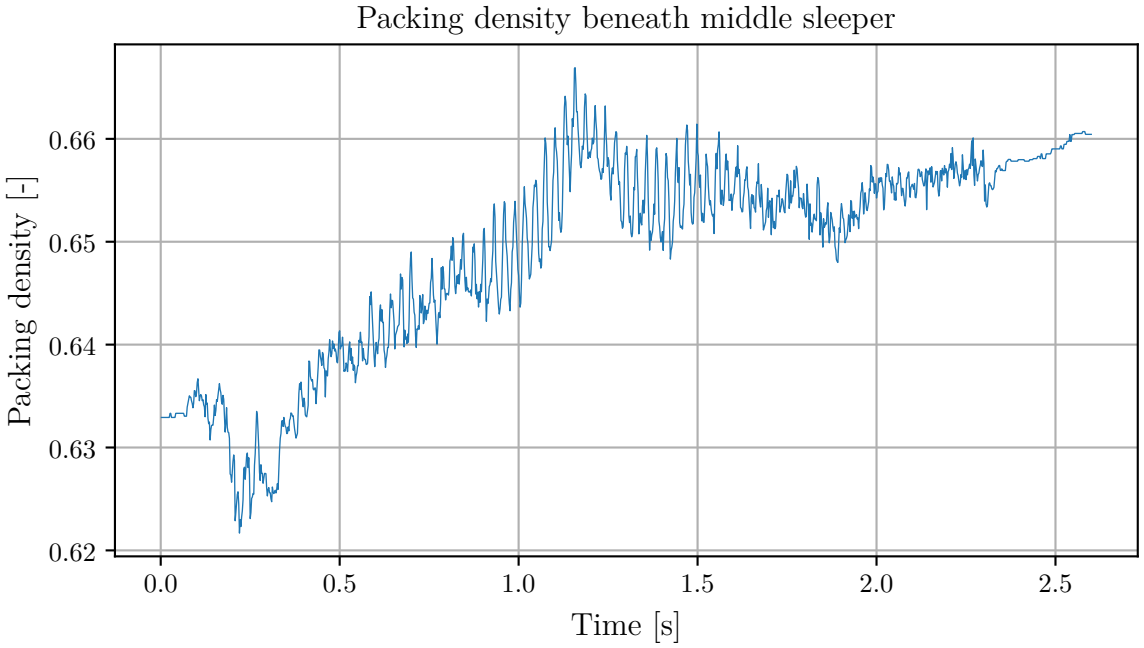

Figure 3.7: Packing density under middle sleeper over time for a compaction time of 3 s.

Vibrations are controlled through the hydraulics for the fully hydraulic tamping model. A sinusoidal function is employed which provides a pressure input to the hydraulic cylinder. This function is given a constant vibrational frequency, while the vibrational amplitude is controlled by a PI regulator that measures the amplitude of the tine vibrations and maintains the amplitude at a constant level. As the tamping tines are retracted, the vibrations are stopped to avoid loosening the compacted

ballast. Stopping the compaction during the tamping cycle is an advantage afforded to hydraulic tamping. Due to the use of an engine to drive the vibrations for a conventional tamping machine, it is not possible to turn the vibrations on and off during the tamping cycle for a conventional tamping machine.

3.2.5 Conventional Tamping

The conventional tamping machine generates vibrations through the use of an eccentric shaft. The shaft is modeled with a constant rotational velocity which gives the desired vibrational frequency. The cylinders are connected to the shaft through revolute joints. These revolute joints are positioned a small distance from the centre of the shaft to achieve the desired amplitude of the tamping tine vibrations. The distance used is dependent on the desired vibrational amplitude. For an amplitude of 5 mm, the distance is set to 3.275 mm.

For the two tamping models, one Simulink model is used where the model may be switched between the fully hydraulic and the conventional tamping model. Figure 3.8 shows the Simulink model.

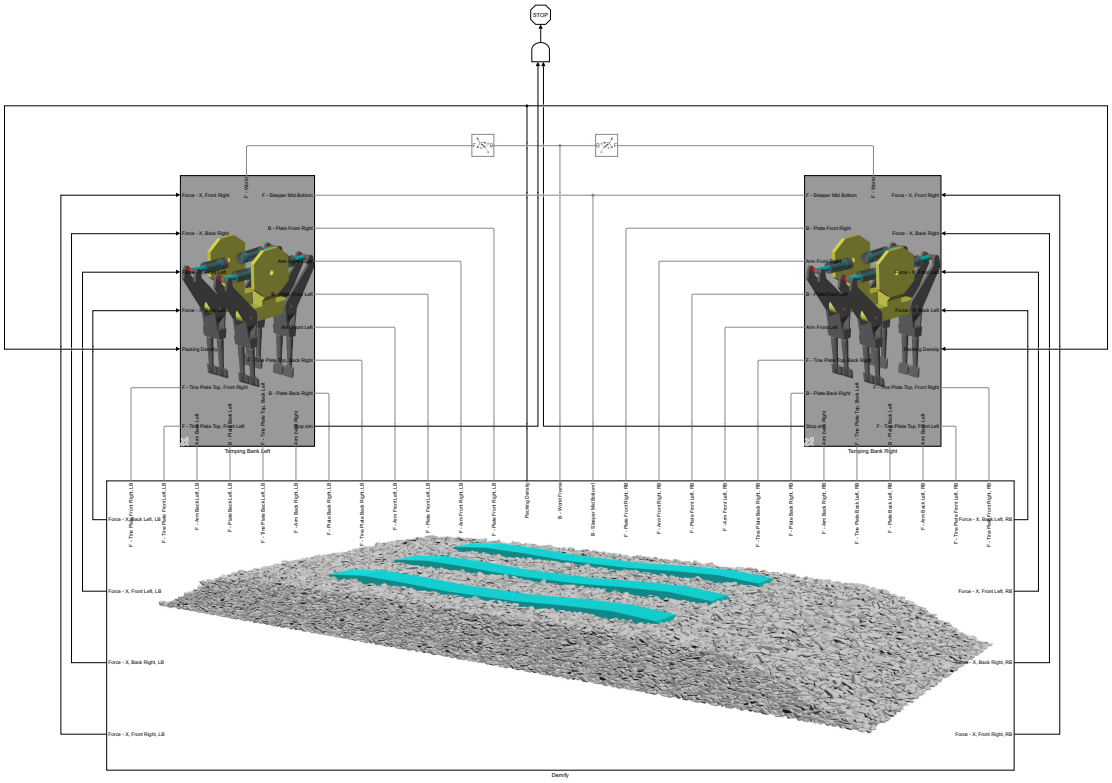

Figure 3.8: Overview of ballast tamping Simulink model

3.3 DEM-MBD Coupling

To control the movement of each rigid object in the DEM simulation, the position and rotation are defined as inputs in the FMU. For each time step in the MBD

solver, the position and rotation are sent to the DEM simulation. This communication poses an issue since the DEM simulation uses a significantly smaller time step, which means that there are several DEM time steps in between each MBD time step. Only updating the position on each MBD time step leads to a coarse discrete movement of rigid objects in the DEM simulation. This issue is alleviated by also including the velocity and rotational velocity of the rigid objects as inputs in the FMU. The velocity allows for a constant movement of the rigid objects in the DEM simulation in between the MBD time steps.

Placing the rigid objects at origin simplifies the coupling between the two simulations. By assuring that origin is defined in the same place in both simulations, the position, velocity, rotation and rotational velocity as seen from origin of each rigid object can be calculated in the MBD simulation and used as input for the FMU. This methodology allows for easy handling of rigid object movements since the objects only have to be defined at origin in the DEM simulation, and everything related to position and movement is controlled through the MBD simulation.

The FMU of the DEM model is imported into the Simulink model. The position, rotation, velocity and rotational velocity of each rigid object are measured in Simulink and used as input for the DEM model. Additional inputs such as DEM time step and the path for the simulation output are controlled through Simulink. The DEM simulation outputs the forces, which are applied to the corresponding MBD object in Simulink.

3.4 Simulation parameters

Nine design parameters are stated in Subsection 2.1.3. The values for these parameters used in both the fully hydraulic and the conventional tamping models are taken from the literature and are presented below [4][3]. The damping coefficient is one other tamping parameter of interest, however, this parameter is a model of all the friction found in the tamping machine decomposed into a single variable. Therefore, there is no value for the damping coefficient available in the literature. Section 5.1 covers the derivation of this value. The time steps for both the DEM and MBD simulations are chosen in Section 4.1 and Section 4.2 respectively.

1. Vibrational frequency = 35 Hz
2. Vibrational amplitude = 5 mm
3. Compaction pressure = 120 bar
4. Compaction time = 1 s
5. Lifting height = 20 mm
6. Penetration depth = 20 mm
7. Penetration speed = 1 m/s
8. Retraction speed = 1 m/s
9. Compaction times = 1

3.5 Parameter study

A parameter study is performed on two different design parameters in order to investigate the effects of the individual parameters on the tamping operation. These parameters along with their respective upper and lower bounds are shown in Table 3.2. Five linearly spaced points are generated for each parameter between the lower and upper bounds and a separate simulation is run for each point. All other design parameters are set to their nominal value shown in Section 3.4. The parameter study is performed for both hydraulic and conventional tamping. The number of points for each parameter refers to the number of points used for one of the tamping models.

Table 3.2: Tamping design parameters used for parameter study.

Parameter	Lower bound	Upper bound	Number of points
Vibrational amplitude [mm]	2	8	5
Vibrational frequency [Hz]	25	55	5

Changing the design parameters may for some values of design parameters cause the tamping operation to perform worse than using the nominal values. In some of these simulations, the packing density may not be able to reach the packing density criterion. To avoid that the fully hydraulic tamping model runs indefinitely due to not reaching the packing density criterion, a second criterion is introduced which places an upper boundary on the compaction time for the fully hydraulic model. This upper bound is chosen as the upper value from the range given by Lichtberger [4]. This criterion is set to 1.2 s.

4
Verification

This section presents the verification of the numerical model in three steps. In Section 4.1, the Rayleigh time step is utilized as guidance in order to choose the DEM time step. Section 4.2 examines the effects of the MBD time step on the co-simulation framework. Finally, in Section 4.3, the ballast bed generation is verified by ensuring that a stationary state has been reached.

4.1 Rayleigh time step

The Rayleigh time step, which is a critical time step used for DEM simulations [29], is calculated in this section. It is useful for setting an upper bound for the DEM time step. The calculation for the critical time step is based on material and geometry parameters of the particles, and as such does not consider the dynamics of the system. These dynamics need to be considered when choosing the DEM time step, and choosing a time step close to the Rayleigh time step does typically not work for a dynamic case. Instead, a DEM time step of roughly 5 % to 20 % of the Rayleigh time step may be used as guidance. The Rayleigh time step dt_R is calculated in the following way, where R is the smallest dilation radius, ρ the density, G the shear modulus, and ν the Poisson's ratio of the particles:

$$dt_R = \frac{\pi R \sqrt{\frac{\rho}{G}}}{0.1631\nu + 0.8766} \tag{4.1}$$

In the DEM simulation, the dilation radius is set as a fraction of the characteristic size of the particle. The fraction applied to all simulations in this thesis is 0.10. The characteristic size is given by the particle size distribution seen in Section 3.1. The smallest characteristic size is 22.4 mm. Thus, $R = 22.4 * 0.1 = 2.24$ mm. Using the calculated value for R along with material parameters found in Table 3.1 (G is calculated from E and ν) the Rayleigh time step is calculated as $dt_R = 2.00\text{e-}5$ s. Due to the large forces acting upon particles restricted in space by other particles, choosing the DEM time step as 5 % is done in order to ensure stability of the simulation, which results in a time step for the DEM simulation of $dt = 1\text{e-}6$ s.

4.2 Co-simulation

In order to choose an MBD time step and to verify the time step independence of the DEM-MBD coupling, meaning that the frequency of communication between the MBD and DEM simulations does not have a significant effect on the results, a simple case consisting of a box filled with spherical particles, together with a tool that moves through the spheres is considered. A visual representation of the case is seen in Figure 4.1.

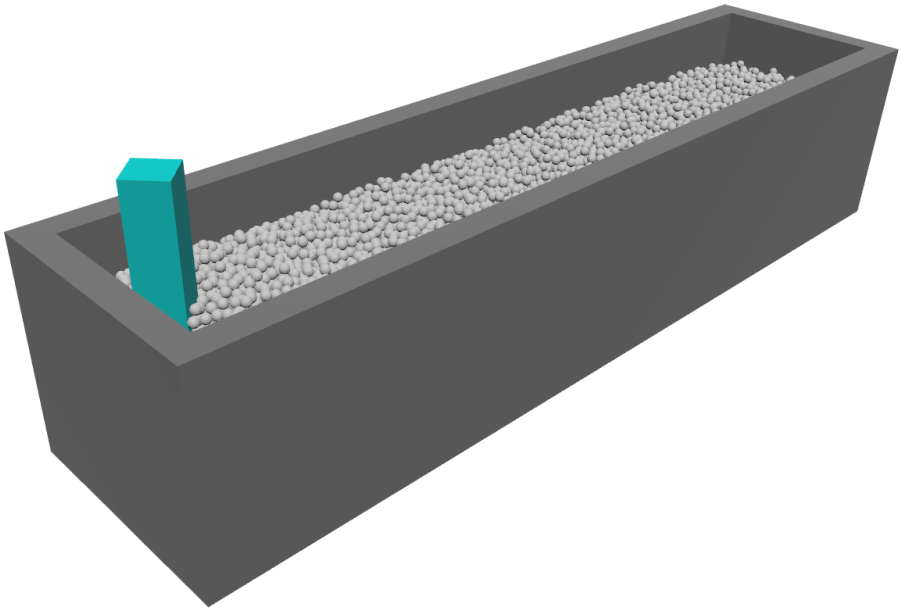

Figure 4.1: Box filled with spherical particles along with movable tool.

The tool moves through the particles at a constant velocity and the norm of the forces acting upon the tool in each MBD time step are recorded. The total kinetic energy of the entire particle population in each MBD time step is also recorded. The time step independence of the co-simulation framework is investigated by analyzing the effects of the MBD time step on the results, since the data transfer between the MBD and DEM simulation is performed at each MBD time step. The verification is performed by comparing the coupled simulations to a pure DEM simulation. The movement of the tool in the pure DEM simulation is set to a constant velocity through Demify®. Secondly, the case is run using the DEM-MBD co-simulation framework where the movement of the tool is set to constant velocity through Simulink. The simulation is then performed for three different MBD time steps. Since the same constant velocity is applied to the tool in all simulations, there should be no difference in the results. Stochastic effects of running the same case using slightly different methods may however occur and the simulations will deviate to some extent. Comparing the magnitude and distribution of the force on the tool and kinetic energy of the particles between simulations is therefore more relevant than comparing the differences in force and kinetic energy signals in time. Figure 4.2 shows the results of the simulations as six histograms. The histograms

show the distribution of both the norm of the force on the tool F_{norm} and the total kinetic energy on the entire particle population for different MBD time steps dt. Each histogram presents both the simulation run through Simulink, using the stated time step, and through Demify®.

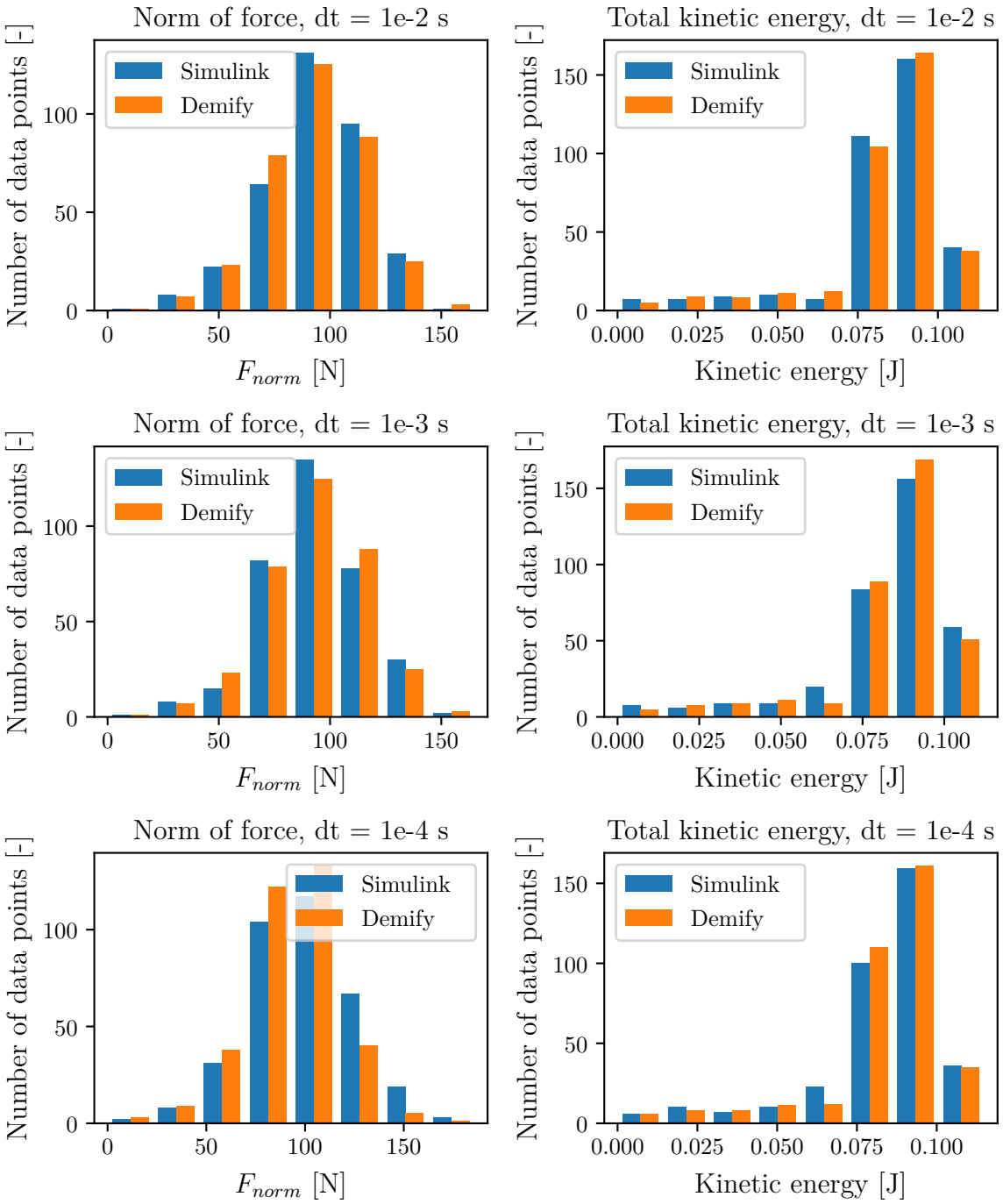

Figure 4.2: Distribution of F_{norm} and kinetic energy for both co-simulations and DEM simulations.

Analyzing the histogram in Figure 4.2 shows that there is no large difference between running the simulation using only DEM or as a co-simulation. Thus, the

different time steps dt have no significant effect on the results either. As previously discussed, there are stochastic effects leading to slight variations between simulations. The distribution and magnitude of the different simulations are however very similar, leading to the conclusion that the DEM-MBD co-simulation framework is time step independent.

The MBD time step dt is chosen as dt = 1e-3 s. Due to the time step independence of the DEM-MBD coupling, the MBD time step may be chosen as a larger size. It is however of great importance that the behaviour of the vibrations of the tamping tines are properly captured in the MBD simulation. A large MBD time step, such as dt = 1e-2 s is not able to properly capture this behaviour due to the sampling frequency being too low. The MBD time step may be compared to the DEM time step, which is dt = 1e-6 s. It is seen that the MBD time step is significantly larger than the DEM time step.

4.3 Ballast bed generation

To ensure that the generated ballast bed has reached a stationary state, the kinetic energy of the entire particle population over time is measured at a frequency of 20 Hz. The evolution of the kinetic energy is then plotted over time, as seen in Figure 4.3. The point in time when the excess particles are removed is also shown with the dashed vertical line. The plot reveals that the ballast bed reaches a stationary state after roughly 5 seconds, beyond the 5 second mark there is only a slight decrease in the kinetic energy.

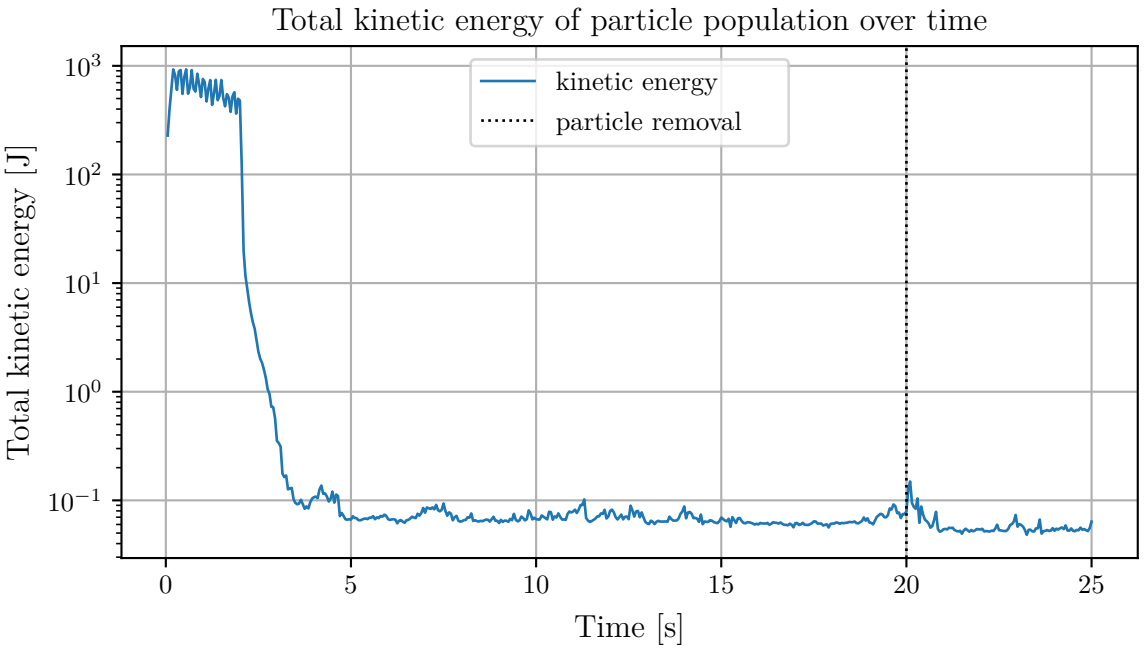

Figure 4.3: Total kinetic energy of particle population during generation.

5
Results

This section presents and analyses the results from the two tamping models along with the results from the parameter study. First, the tamping model is validated against real-world data in Section 5.1, then, the effects of different values for the packing density criterion are explored in Section 5.2. In Section 5.3, the two tamping models are evaluated and compared. Lastly, the results from varying operational parameters are presented and analyzed in Section 5.4.

5.1 Validation

The fully hydraulic tamping model described in Chapter 3 is validated against real-world data from System7's online tool Inframe, where data from a fully hydraulic tamping machine is logged during the tamping operation. This data is provided to this project through Infranord. It is important to note that the data from Inframe is only representative of the fully hydraulic tamping model, and as such, only the fully hydraulic model is validated against the data. The data of interest for validation purposes are *compaction force* and *squeeze path*. These two variables are measured in the tamping cylinders, where the compaction force is the average value of maximum forces measured in each individual cylinder. Similarly, the squeeze path is the average value of the maximum travel distance measured in each individual cylinder. The compaction force and squeeze path are calculated from the fully hydraulic tamping model and compared to data taken from Inframe. This data is chosen among ballast beds with low stiffness. Due to the lack of compaction in the modeled ballast bed, it is representative of a real-world ballast bed with low stiffness. The fully hydraulic tamping model does not use the previously established tamping criterion in the validation, instead, a compaction time of 0.8 s is applied, which is a rough estimate of the compaction time of a typical tamping operation by a fully hydraulic tamping machine [21].

The fully hydraulic tamping model is validated against a distribution of tamping operations to ensure that the model results are within the expected range found in real-world tamping operations. Due to a large number of variables prevalent in a real-world tamping operation, such as ballast bed condition, operator settings, weather and specific machine model, validating against one tamping cycle is not reasonable due to the large spread of results from different operations.

The damping coefficient ξ_{cyl} previously described in Subsection 3.2.1 has a direct

influence on both the compaction force and the squeeze path. A low damping coefficient leads to low friction in the MBD model, which gives a high squeeze path and a high compaction force, while a high damping coefficient leads to high friction giving a low squeeze path and a low compaction force.

The damping coefficient is investigated through a parameter study where the coefficient is varied by considering 13 points between 8e5 N/ms and 1.6e6 N/ms. The remaining design parameters are set to their nominal values shown in Section 3.4. Figure 5.1 shows the results of this parameter study. Analyzing the plots shows that ξ_{cyl} has a direct influence on both the squeeze path and compaction force. At low values of ξ_{cyl}, the compaction force is very high at over 100 kN. This high compaction force is due to the tamping tines being close to the sleeper and squeezing single particles in between the tine and the sleeper. In a real-world scenario, this high force would cause these particles to fracture, thus lowering the compaction force. However, due to the absence of a particle breakage model in the numerical simulations, this phenomenon is not observed and results instead in a very high compaction force. As $\xi_{cyl} >$ 1e6 N/ms the compaction force starts to converge towards 11 kN due to the tines being further away from the sleeper. The squeezing path decreases almost linearly, from the peak at 70 mm to the minimum at 30 mm, and does not converge.

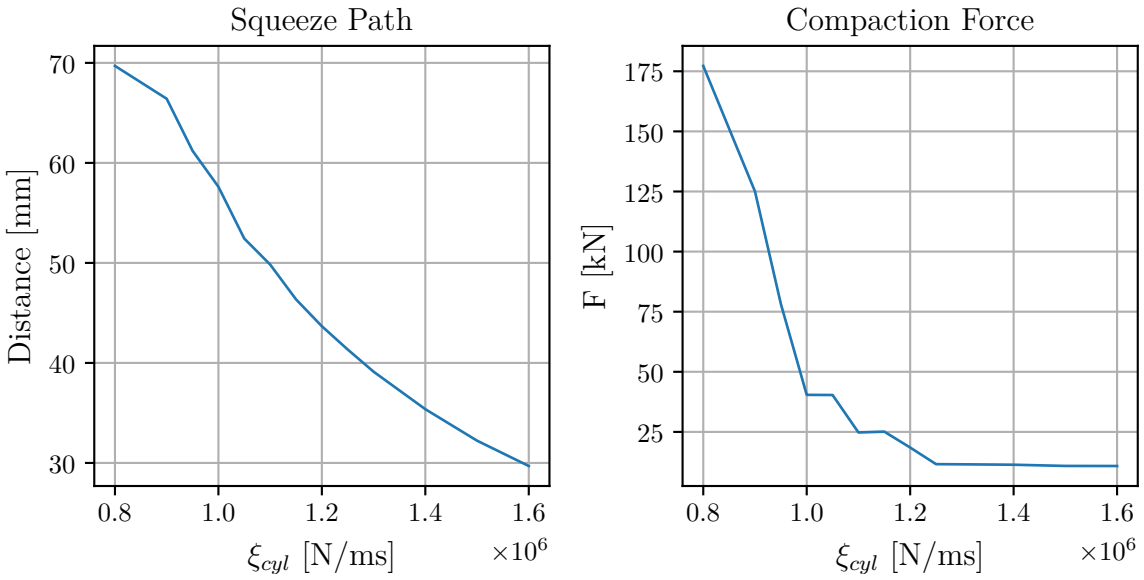

Figure 5.1: Parameter study of cylinder damping coefficient ξ_{cyl} with the squeeze path (left) and the compaction force (right)

In order to find the damping coefficient value that most accurately represents a real-world tamping machine, 1907 data points are extracted from Inframe and the compaction force and squeeze path distribution of this data is visualized as two histograms, seen in Figure 5.2. The results from the damping coefficient parameter study are highlighted in these plots.

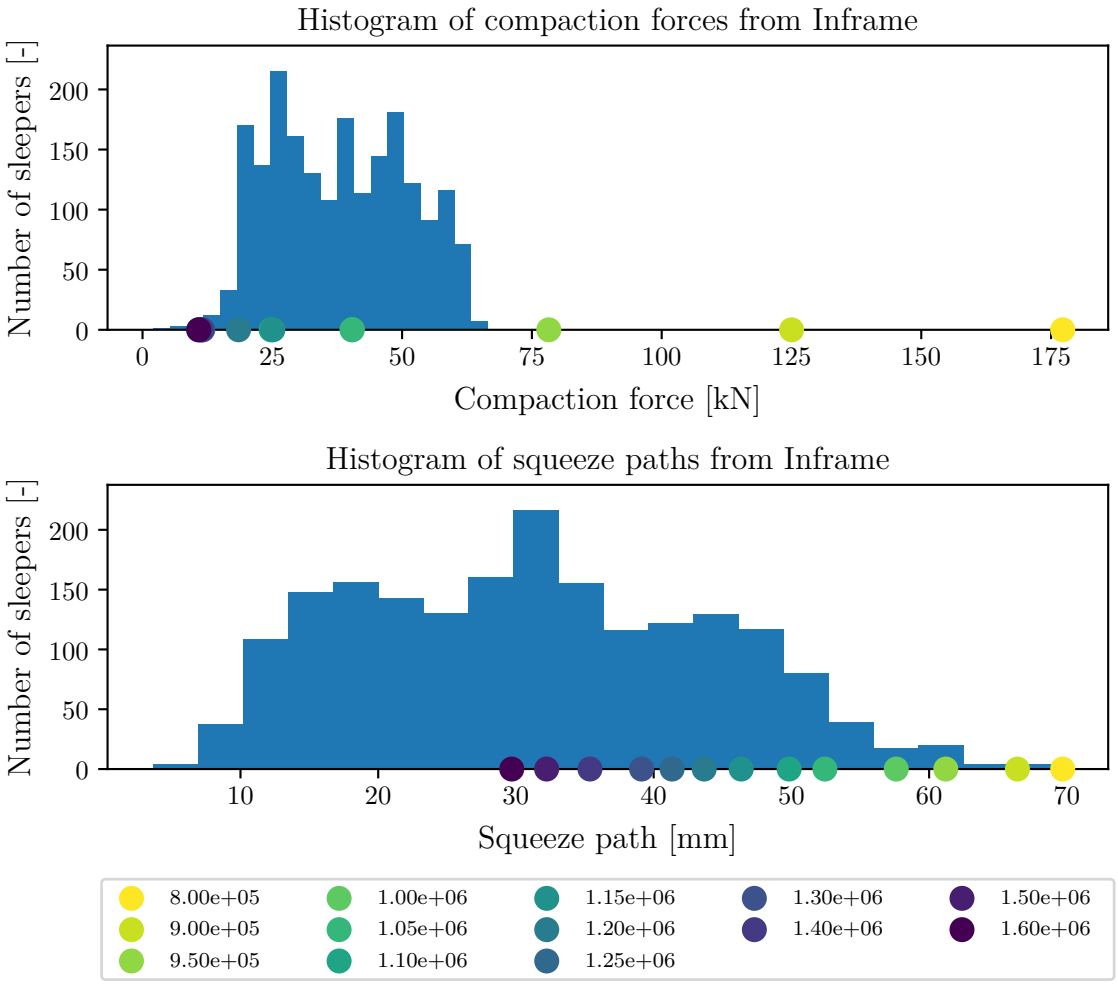

Figure 5.2: Distribution of compaction force and squeeze path along with results from parameter study of cylinder damping coefficient ξ_{cyl}.

A simulation result close to the mean of both distributions is desirable to achieve a model that is representative of real-world tamping operations. Therefore, the mean and standard deviation of both the histograms are calculated. For each simulation, the number of standard deviations from the mean, n_{std}, of the histograms are calculated and visualized in Figure 5.3 as a function of the damping coefficient ξ_{cyl}. Finding the minimum n_{std} for the two variables is done in order to find the point closest to the mean of the two distributions. However, these minimums do not coincide, therefore the optimal ξ_{cyl} is evaluated by the norm of the number of standard deviations from the mean. The optimal value ξ_{cyl} is then the minimum of this norm, which is calculated as follows:

$$n_{std,norm} = \sqrt{n_{std,f}^2 + n_{std,sp}^2} \tag{5.1}$$

Where $n_{std,f}$ refers to the number of standard deviations from the mean for the compaction force and $n_{std,sp}$ for the squeeze path. $n_{std,norm}$ as a function ξ_{cyl} is visualized in Figure 5.3.

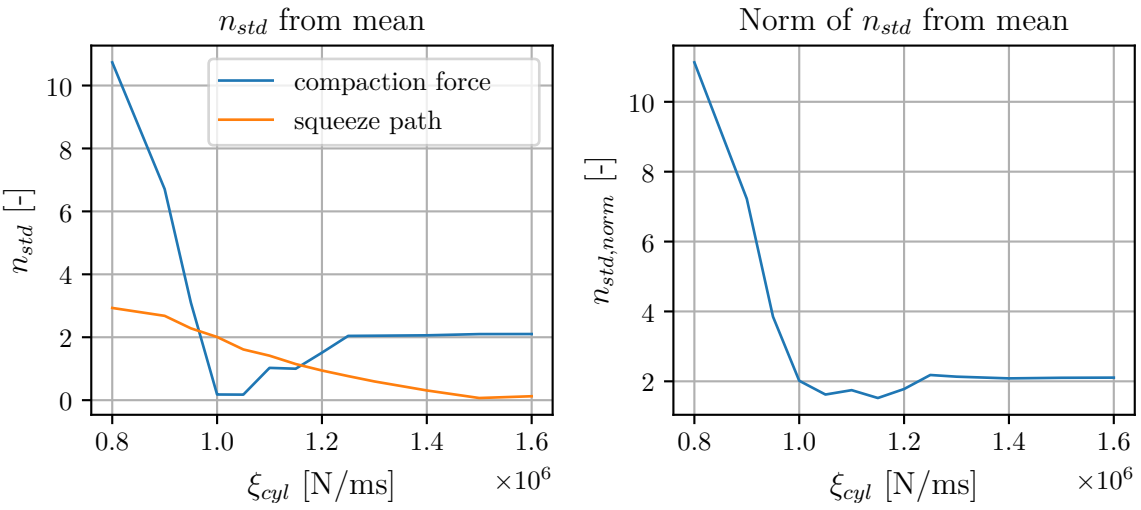

Figure 5.3: Number of standard deviations from the mean.

The minimum of $n_{std,norm}$ is found at $\xi_{cyl} = 1.15 \times 10^6$ N/ms. This point is shown as a dashed vertical line together with the histograms from the Inframe data in Figure 5.4 to show that the model is within the expected distribution of a real-world tamping machine.

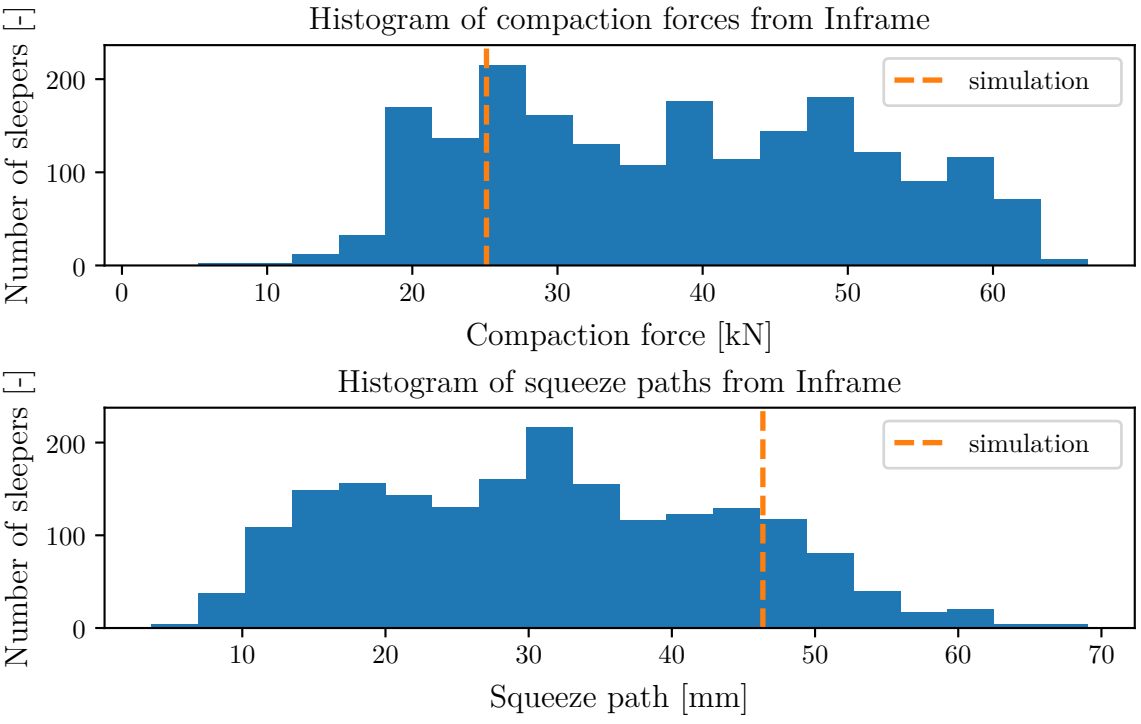

Figure 5.4: Distribution of compaction force and squeeze path along with validated simulation results.

No data from a conventional tamping machine is available for the purposes of this thesis, and as such, only the fully hydraulic tamping model is validated, not the conventional tamping model.

5.2 Packing Density Criterion

Two different values are considered for the packing density criterion: $pd_c = 0.655$ and $pd_c = 0.66$. The reasons for choosing these values are stated in Subsection 3.2.4. One simulation for each of the pd_c values is performed with the nominal values for all other tamping parameters found in Section 3.4.

As described in Subsection 2.1.5, there are various approaches to quantifying the effectiveness of the tamping operation. One of the approaches is to evaluate the ability of the ballast bed underneath the sleeper to transfer load from the sleeper to the subballast. This may be indirectly measured by evaluating the packing density and the forces acting upon the sleeper, both of which are presented in this section.

The packing density underneath the middle sleeper is measured in the same manner as described in Subsection 3.2.4 for both values and compared in Figure 5.5.

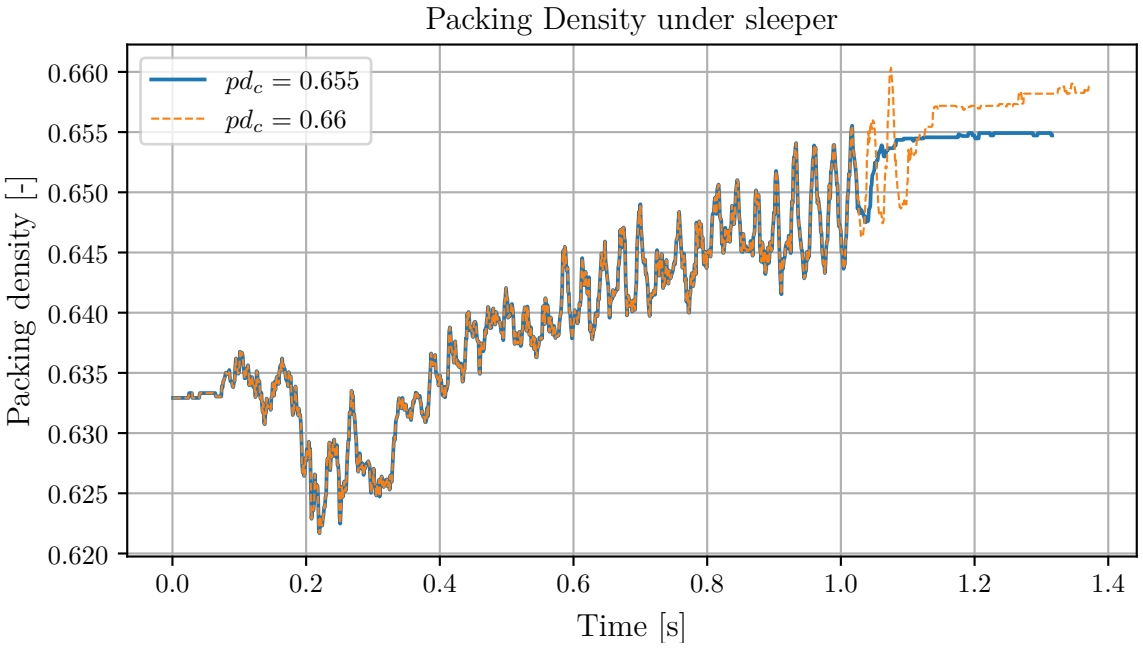

Figure 5.5: Packing density underneath middle sleeper for different pd_c values.

It can be seen that the packing density stabilizes close to 0.655 for $pd_c = 0.655$ and close to 0.658 for $pd_c = 0.66$. Therefore, $pd_c = 0.66$ is preferable since it yields a higher final packing density.

A large force acting on the sleeper along the z axis gives an indication as to how many ballast particles are in contact with the sleeper and the ability of the ballast bed to transfer loads from the sleeper to the subballast. Conversely, a large force acting on the sleeper may also indicate a large risk of particle breakage beneath the sleeper. The forces acting on the middle sleeper along the z axis for both pd_c values are presented in Figure 5.6.

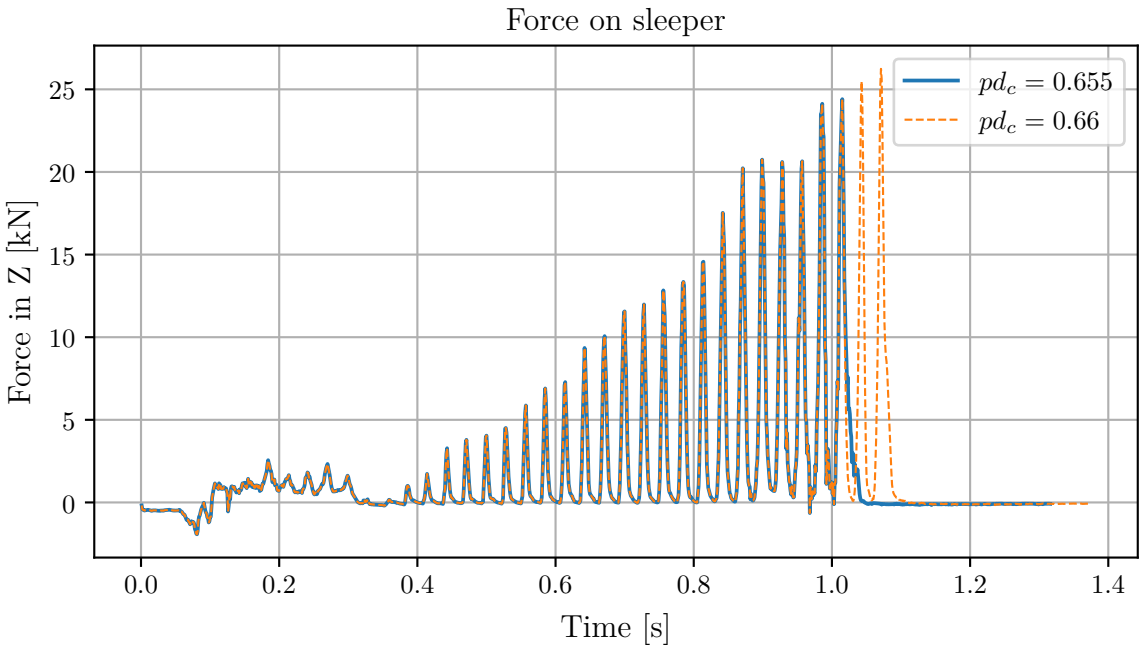

Figure 5.6: Force along z axis acting on middle sleeper for different pd_c values.

The higher value of pd_c yields two additional vibration cycles as compared to the lower value, this gives a slight increase in the force acting upon the sleeper. This small increase in force may point towards more particles being in contact with the sleeper from below and/or particle breakage being more likely underneath the sleeper. This increase in force is however small enough that no clear conclusions can be drawn from it. It is important to note here that the sleeper is fixed in place, the forces acting upon the sleeper would in a real-world scenario cause some movement of the sleeper.

The previous two plots indicate that the higher pd_c value is beneficial. However, the adverse effects of applying a higher packing density criterion should also be explored to ensure that the higher pd_c value does not lead to increased degradation of the ballast bed condition.

The effects of the tamping cycle on the ballast particles are mainly measured by analyzing the forces affecting the particles. Presenting the forces on the ballast particles is a non-trivial task due to the large number of ballast particles. Further, the vast majority of the ballast bed particles is not directly interacting with the tamping tines and thus will only experience low forces.

The maximum force upon a single particle during the entire tamping operation is of most interest, as compared to the entire history of the force acting upon said particle. The maximum force experienced by each particle is thus calculated and all the maximum forces are presented in Figure 5.7 through a histogram, showing the distribution of the forces. This plot is in log-log scale due to the previously explained phenomena of the vast majority of particles experiencing low forces.

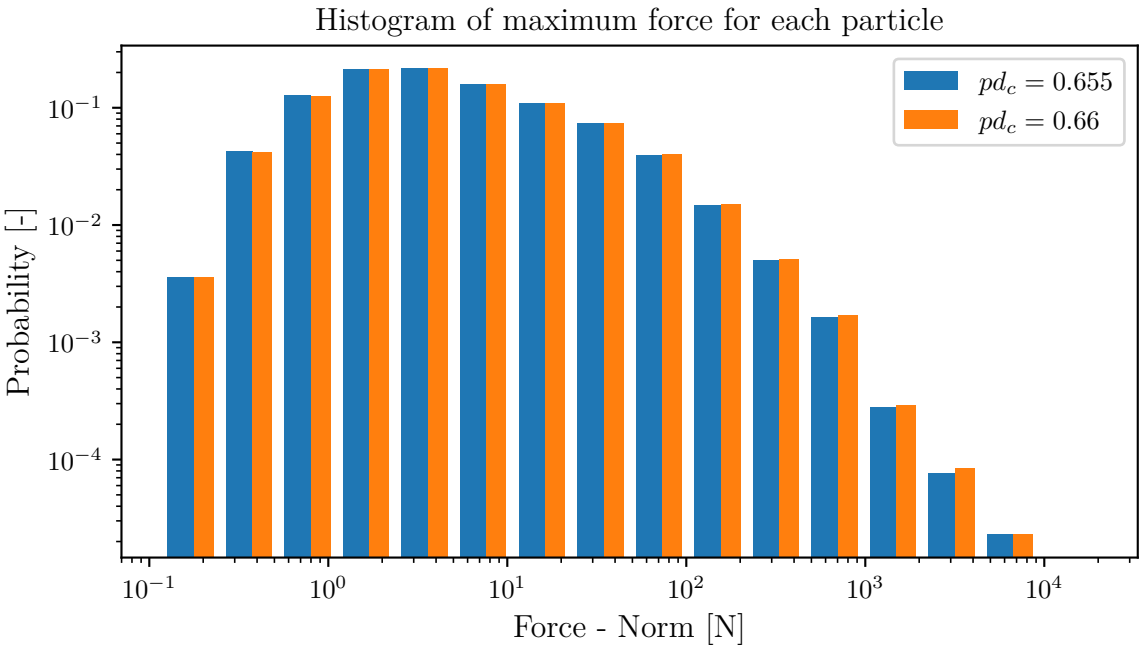

Figure 5.7: Distribution of maximum force acting upon each particle for different pd_c values.

The figure shows that the vast majority of particles experience force below 10 N and only a few particles experience force above 1 kN with the maximum force being below 10 kN. It is clear from the figure that there is no significant difference in the forces acting upon the ballast particles between the two values of pd_c. Due to the higher value of pd_c yielding a higher final packing density, with no clear downsides, it is chosen for the fully hydraulic model used in the comparison and the parameter study.

5.3 Comparison

In this section, the results of the tamping process are compared for the fully hydraulic and the conventional simulation model. For both, all tamping parameters are chosen as their nominal values found in Section 3.4. It is important to note here, that all design parameters are applied for both models, except compaction time, which is only relevant for the conventional tamping model. However, the packing density criterion is only utilized in the fully hydraulic model. All figures in this section present results from both models to facilitate the comparison between them. The same types of visual representation of the results presented in Section 5.2 are used for the comparison of the fully hydraulic and the conventional tamping model, along with additional figures to provide a deeper analysis.

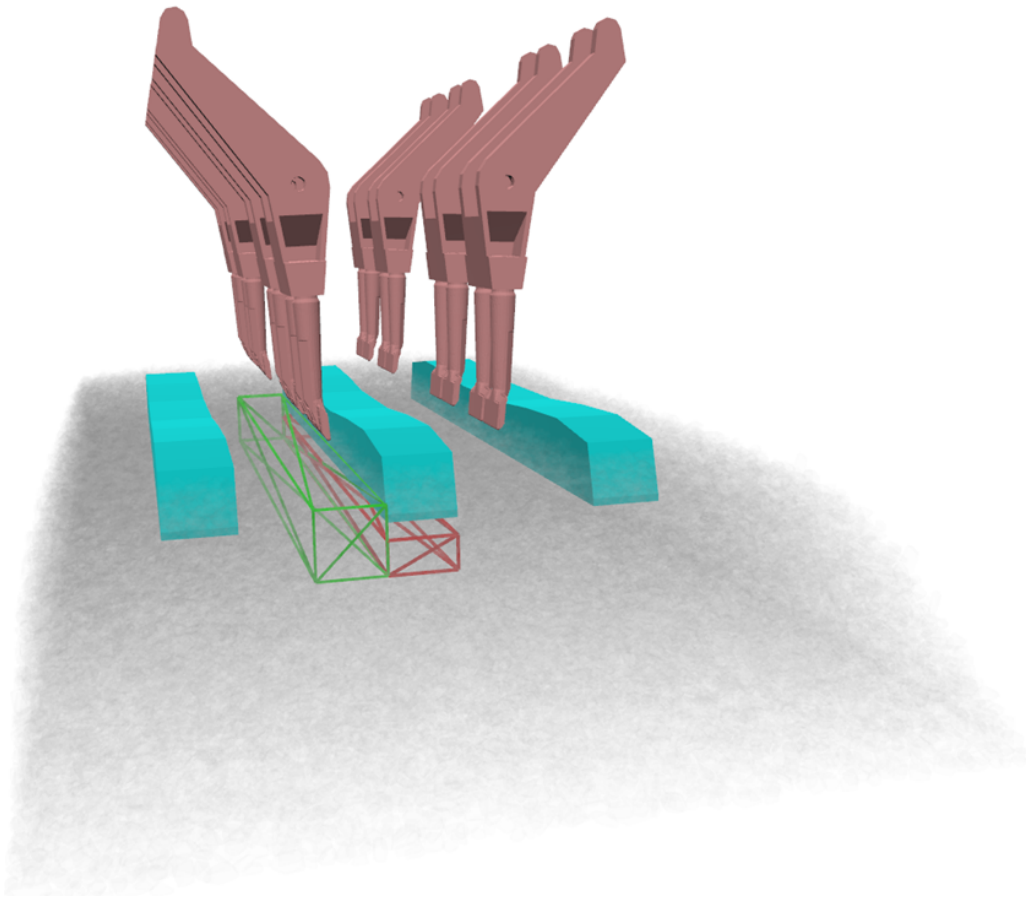

Figure 5.8: Volume for measuring packing density under sleeper (red) and beside sleeper (green).

The packing density is measured beneath the middle sleeper. Further, it is also measured in the ballast to the side of the sleeper to investigate the effects of the tamping operation on the ballast situated in between the sleepers. The two volumes where the packing density is measured are shown in Figure 5.8 The two packing densities for both tamping models over time are given in Figure 5.9.

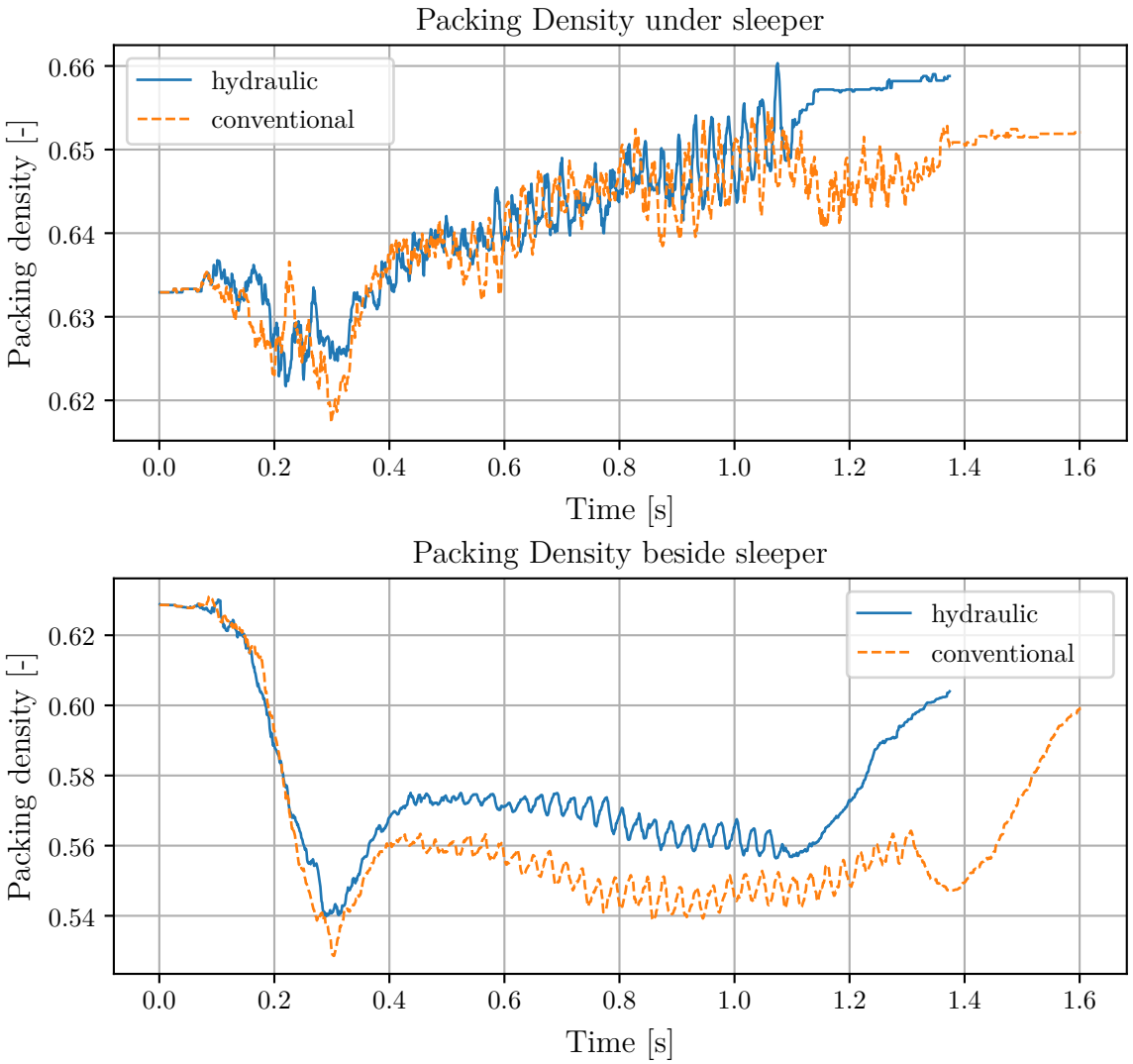

Figure 5.9: Packing density beneath the middle sleeper (top) and beside the sleeper (bottom) for both tamping models.

The packing density underneath the sleeper shows that for both tamping models, the initial packing density is disturbed by the tamping tines being inserted into the ballast bed. Further, the packing density for both of the models rises at roughly the same rate once compaction is begun, however, the packing density for the conventional tamping model does not reach the same packing density as the fully hydraulic model at the end. At roughly 1.1 s into the simulation, the packing density starts to drop for the conventional model. There is a large decrease in the packing density beside the sleeper as the tamping tines are inserted into the ballast bed. This is due to the packing density only measuring the volume of the ballast particles, and not the tamping tine. Thus, the presence of the tines lowers the packing density. After the tines are removed from the ballast bed, the packing density increases again. It does not however increase to the initial level, showing that the tamping operation causes a significant disturbance in the ballast bed beside the sleeper. The packing density beside the sleeper for the conventional tamping model decreases to a lower level during the compaction and reaches a lower final packing density as compared

to the fully hydraulic model. These two plots show that the fully hydraulic tamping model manages to achieve a higher packing density than the conventional model, both underneath and to the side of the sleeper.

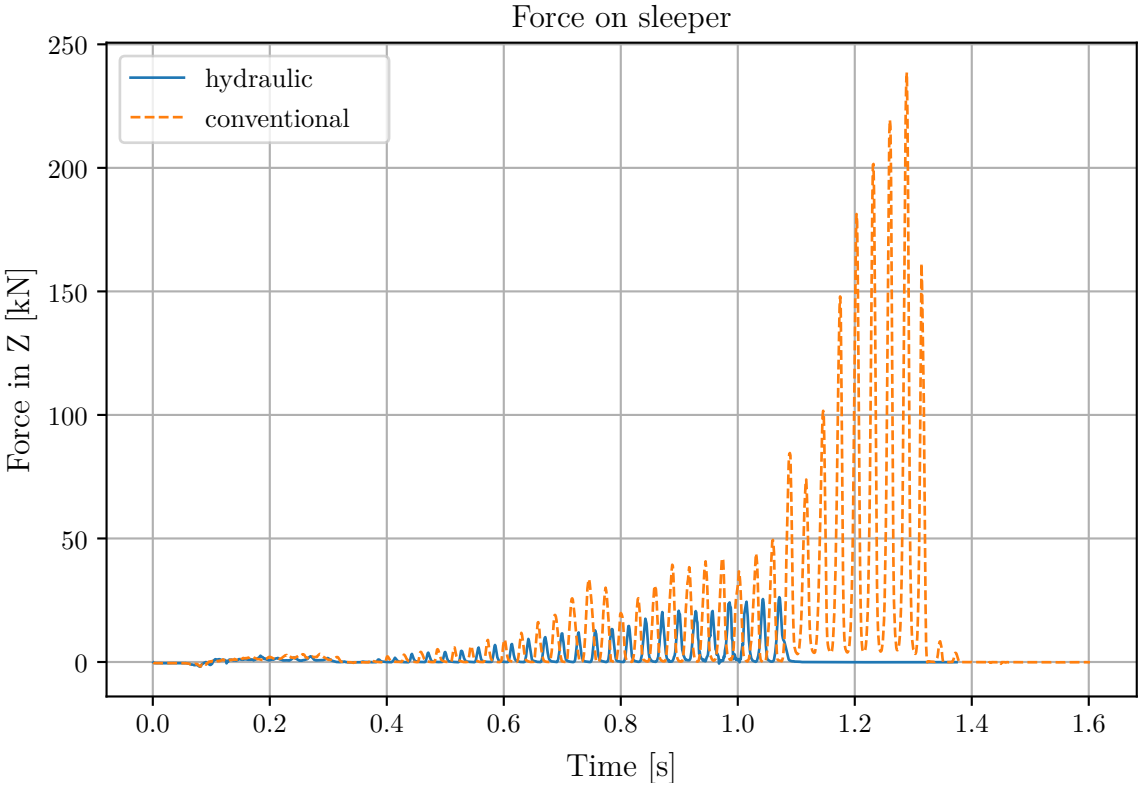

Figure 5.10: Force in z acting on the middle sleeper for both tamping models.

The force acting upon the sleeper along the z axis is visualized in Figure 5.10 for both tamping models. The figure shows that for both tamping models, the forces on the sleeper steadily increase with each vibration cycle until roughly 1.1 s, presumably due to the higher packing density beneath the sleeper along with the tamping tines moving closer to the sleeper. After 1.1 s, the fully hydraulic tamping model stops the compaction and vibration, thus the force on the sleeper is reduced. For the conventional model, the force is higher than the hydraulic one before 1.1 s with a factor of roughly two. After 1.1 s however, the force gets very large, reaching over 200 kN. Due to the absence of a particle breakage model in the simulation, there is a risk of ballast particles being lodged in between the sleeper and the tamping tines, leading to an exceedingly high force on the sleeper. In a real-world tamping operation, this large force would be likely to cause some particle breakage from particles in contact with the sleeper and the tines, along with movement of the sleeper. For these reasons, the observed behaviour may be regarded as unphysical and further conclusions from the figure are hard to draw.

The distribution of all individual particles' maximum force experienced throughout the tamping operation for both tamping models are presented in Figure 5.11 as a density histogram with 16 bars. An important note here is that both axes of the figure are in logarithmic scale.

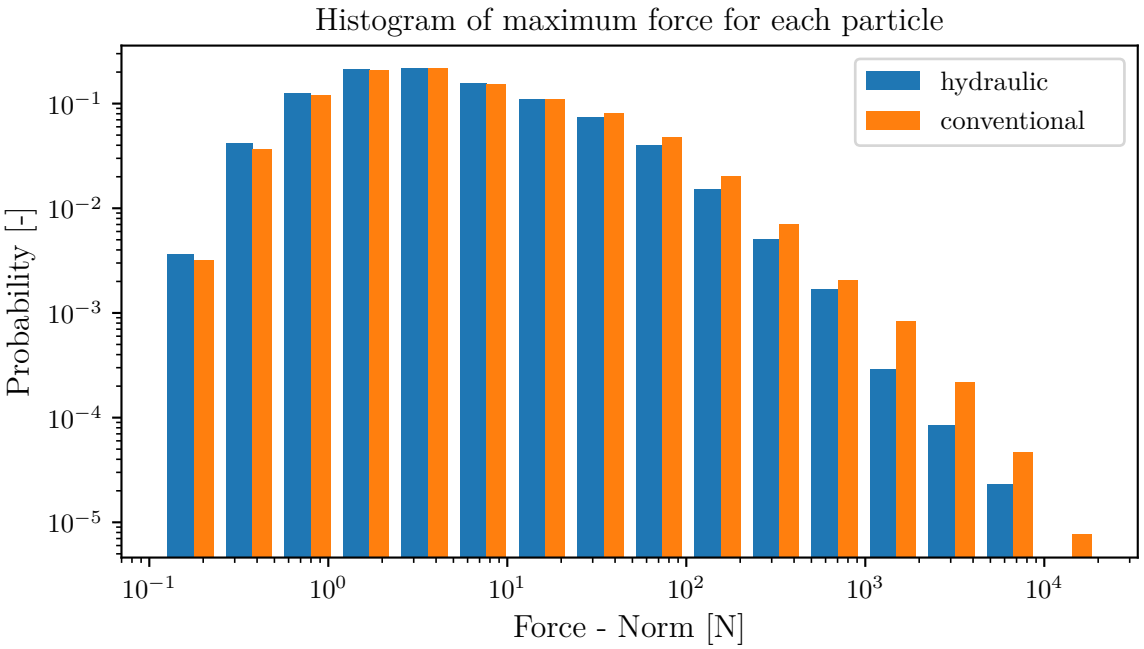

Figure 5.11: Distribution of maximum force acting upon each particle for both tamping models.

It can be seen in the histogram that for the hydraulic tamping model, there are more particles with a lower maximum force while there are fewer particles with a higher maximum force as compared to the conventional tamping model. From the figure, it can be seen that there are more particles experiencing a force under 1 N for the fully hydraulic method than the conventional method. Conversely, there are more particles experiencing forces above 20 N for the conventional model than the fully hydraulic one, with there only being particles above 10 kN for the conventional model. It is clear from analyzing the figure that the conventional tamping model exerts a higher force on the particle population than the fully hydraulic model.

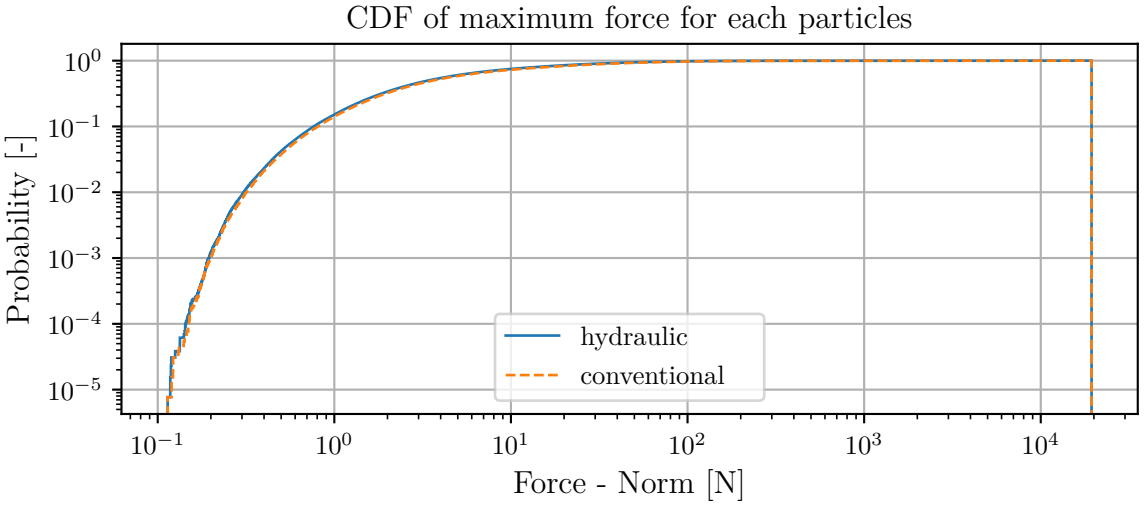

Figure 5.12: CDF of maximum force acting upon each particle for both tamping models.

Another approach to presenting the forces applied to the particles is through a cumulative distribution function (CDF). The CDF of the maximum force for each particle is shown in Figure 5.12. Even though the figure is in log-log scale, it is not possible to see any significant difference between the two CDFs. It may however be seen that for both tamping models, very few particles experience a force above 100 N. One way to analyze and compare different CDFs is to find the value at a certain probability for both CDFs and compare them. For example: the force found at 90 %. Eight different probabilities are chosen and the force found at these points for both tamping models are presented in Table 5.1. Due to the higher level of force being of interest to investigate the risk of particle breakage, and the large number of particles experiencing low levels of force, the table includes values found towards the upper end of the distribution.

Table 5.1: Values taken from the CDF for both tamping models

Probability [-]	F [N] - Hydraulic	F [N] - Conventional
90	30.44	36.88
95	55.56	69.08
99	167.59	213.82
99.5	268.14	332.54
99.9	639.49	987.66
99.95	872.45	1427.58
99.99	2124.11	3155.22
99.995	3330.86	4430.24
99.999	5374.50	7691.59

The table shows that for all chosen probabilities, the conventional tamping model affects the ballast particles with a higher force than the fully hydraulic tamping model. The differences in force between the models are not very large for the lower probabilities such as 90 % and 95 %. However, from 99.95 % and up, the force from the conventional model is around 50 % larger than the force from the hydraulic model, showing that there is a large difference between the models.

5.4 Parameter Study

In this section, the results of the parameter study of selected tamping design parameters are shown. Studies for two different parameters are presented: vibrational amplitude (Subsection 5.4.1) and vibrational frequency (Subsection 5.4.2). The results from the different studies are given in the same manner for all parameters, which assists the comparison between the parameter results. This in turn facilitates a discussion surrounding the effects of the different parameters on the tamping process.

Firstly, the compaction time is presented. The compaction time for the fully hydraulic model varies depending on if and when the packing density criterion is reached. For the conventional model, the compaction time is constant, thus, the

compaction time is mainly relevant for the fully hydraulic model.

Secondly, six variables are defined to evaluate the results of the parameter study. Due to the large number of simulations involved in the study, six different scalar measures are introduced to facilitate the evaluation of the entire parameter study. For example, analyzing the packing density evolution over time for each simulation is difficult and it may be easier to analyze the final packing density for all simulations instead. These scalar variables are defined and described below.

Two of the six scalar measures are defined in order to evaluate the forces acting upon the ballast particles. These are: the number of particles experiencing a force over 500 N and the force found in a CDF of the maximum force upon each particle at 99.99 %, similar to the values found in Table 5.1. Since the main focus of the parameter study is to evaluate how the results respond to different values of the design parameters, the differences between the results of different simulations are of greater interest than the value of the results of each individual simulation. Therefore, the specific value used to define the scalars does not matter much, as long as the measures reflects the results of the tamping operation.

The compaction force and squeeze path are also employed for evaluation of the results. These two measures point towards the movement of the tamping tines and the forces acting upon the tines. The access to real-world data, as seen in Section 5.1, provides insight into how changing the design parameters affects the relation between the tamping models and a real-world tamping operation.

Finally, the packing density is evaluated through two measures: the final packing density and the minimum packing density, both evaluated underneath the middle sleeper as described in Subsection 3.2.4. The final packing density describes how effective the tamping operation is at compacting the ballast underneath the middle sleeper, and the minimum packing density gives insight into how much the ballast bed is disturbed upon penetration of the tamping tines.

In the following sections, the values for these six measures are presented and analyzed for each design parameter.

5.4.1 Vibrational amplitude

The compaction time for different vibrational amplitudes is shown in Figure 5.13. For the fully hydraulic tamping model, amplitudes of 2 mm and 3.5 mm do not reach the packing density criterion. The minimum compaction time is given from amplitudes of 5 mm and 8 mm. The packing density criterion is reached after 0.8 s for these two points. For the conventional tamping model, the compaction time is constant which is seen in the figure.

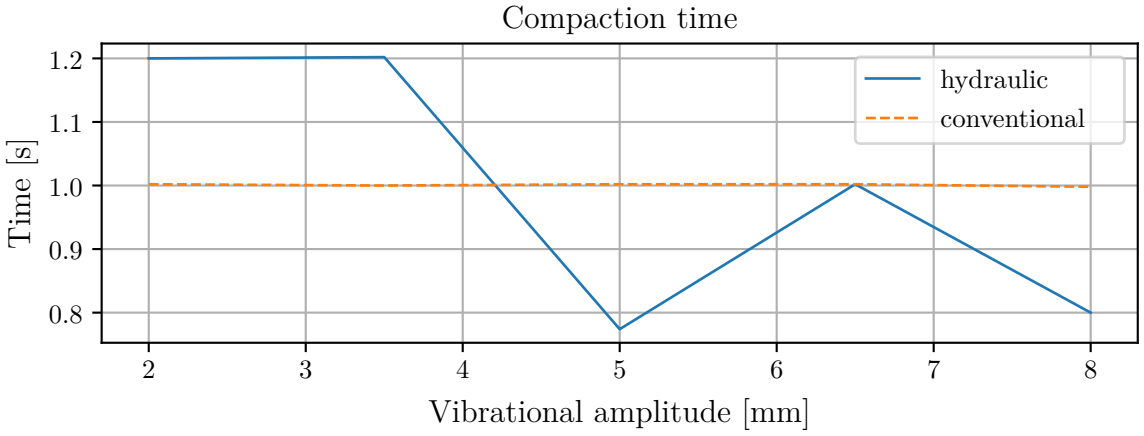

Figure 5.13: Compaction time for different vibrational amplitudes.

As described above, the forces acting upon the particles are evaluated through the number of particles experiencing a force over 500 N and the force found in a CDF of the maximum force upon each particle at 99.99 %. These results, for both the hydraulic and the conventional tamping models, are seen in Figure 5.14.

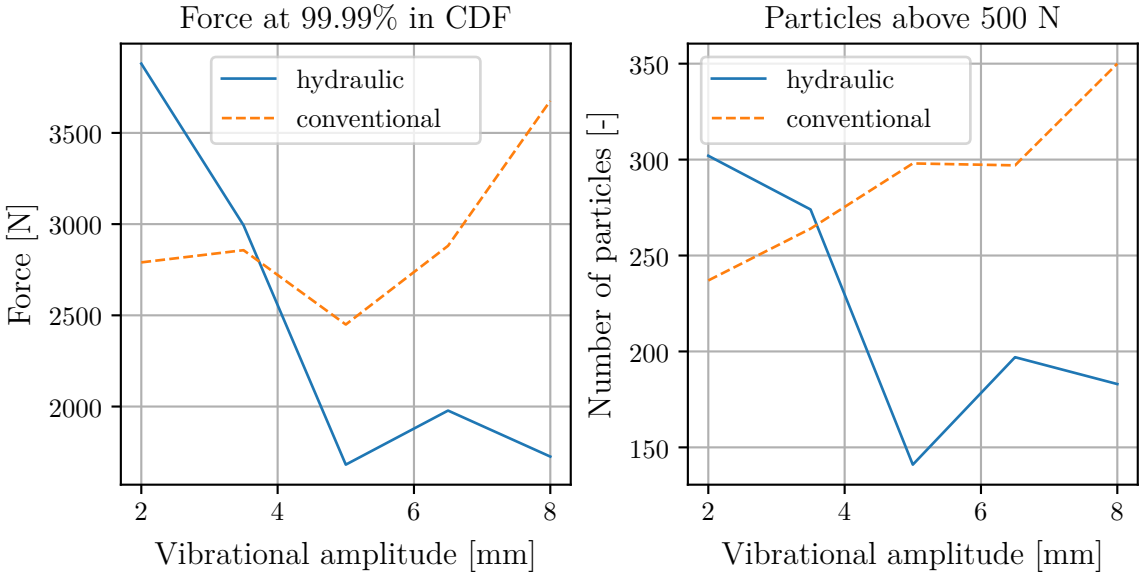

Figure 5.14: Forces acting upon particles for different vibrational amplitudes.

For the fully hydraulic model, it can be seen that high levels of force affect the particles when the amplitude is below 5 mm, while the amplitudes above 5 mm do

not have the same effect on the forces. This behaviour is due to the differences in compaction time, i.e. the lower amplitude values have a significantly longer compaction time compared to the higher amplitude values. A vibrational amplitude of 5 mm is optimal for the fully hydraulic model, followed by 8 mm. For the conventional tamping model, the compaction time is constant, and as such, the results are not dependent on the compaction time. The higher force levels for the conventional model are found for an amplitude of 8 mm. Generally, the forces increase with the vibrational amplitude except for an amplitude of 5 mm where the force at 99.99% from the CDF is minimized.

The compaction force and squeeze path for both the hydraulic and the conventional tamping models are seen in Figure 5.15.

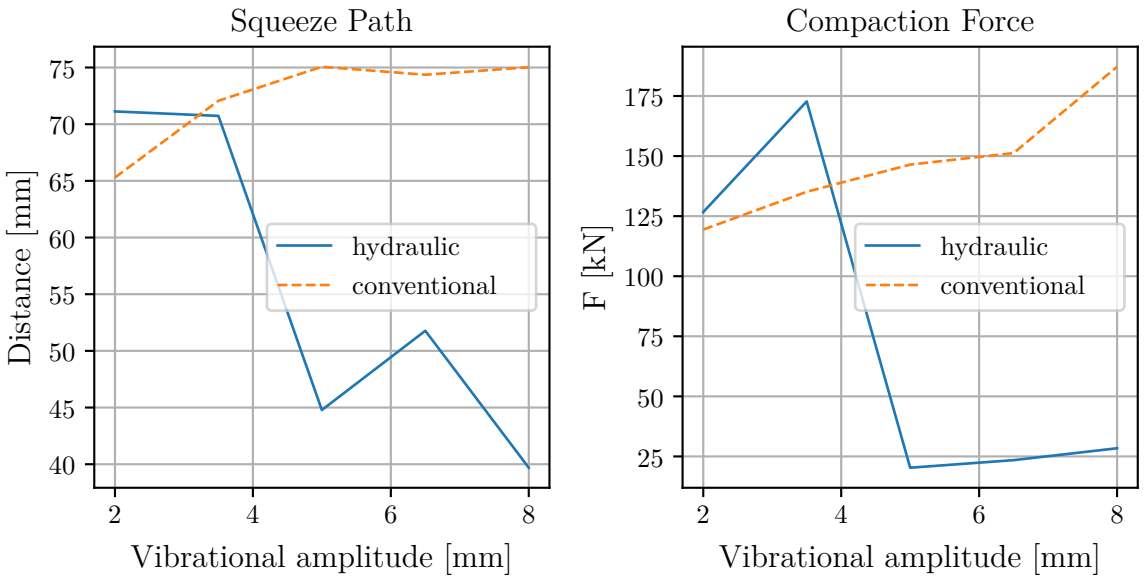

Figure 5.15: Squeeze path and compaction force for different vibrational amplitudes.

The squeeze path and compaction force magnitudes are similar for the conventional tamping model and for the fully hydraulic tamping model when the amplitude is lower than 5 mm. Both the squeeze path and the compaction force are significantly higher for the low amplitudes of the hydraulic model and for the conventional model. The lower squeeze path and compaction force for the fully hydraulic model show that when the packing density criterion is reached, the compaction force and squeeze path decrease significantly. The minimum compaction force is found at an amplitude of 5 mm for the fully hydraulic model. Both the squeeze path and the compaction force are seen to increase with the amplitude for the conventional model.

The final and the minimum packing density for both the hydraulic and the conventional tamping models are seen in Figure 5.16.

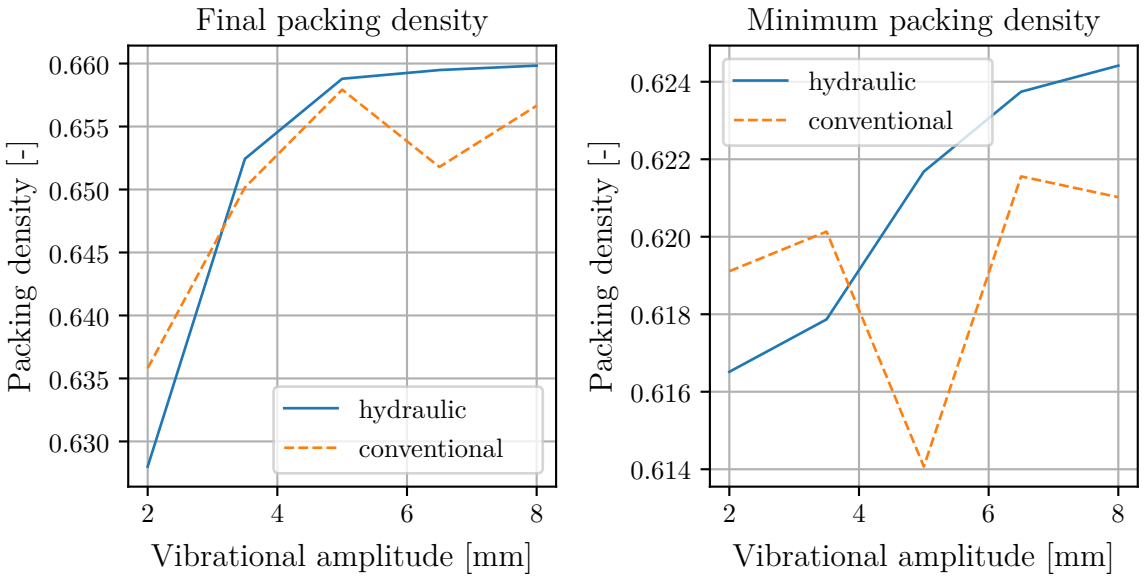

Figure 5.16: Final and minimum packing density for different vibrational amplitudes.

For the fully hydraulic tamping model, both the final and the minimum packing density increase with the vibrational amplitude, showing that an increased amplitude is beneficial for maximizing the packing density underneath the middle sleepers. A similar behaviour is observed for the conventional tamping machine, however with a minor decrease in final packing density at an amplitude of 6.5 mm and a major decrease in the minimum packing density at an amplitude of 5 mm. These results show that the fully hydraulic tamping model yields a more compacted ballast bed underneath the middle sleeper for vibrational amplitudes over 3.5 mm as compared to the conventional model. The results also point towards the packing density converging for high amplitude values.

5.4.2 Vibrational Frequency

The compaction time for different vibrational frequencies is shown in Figure 5.17. For the fully hydraulic tamping model, the packing density criterion is not used for frequencies of 25 Hz and 40 Hz. For 32.5 Hz, the packing density criterion is reached at roughly 1.1 s, which is very close to the maximum compaction time of 1.2 s. For higher frequencies, the compaction time is significantly reduced. As previously mentioned, the compaction time for the conventional tamping model is constant

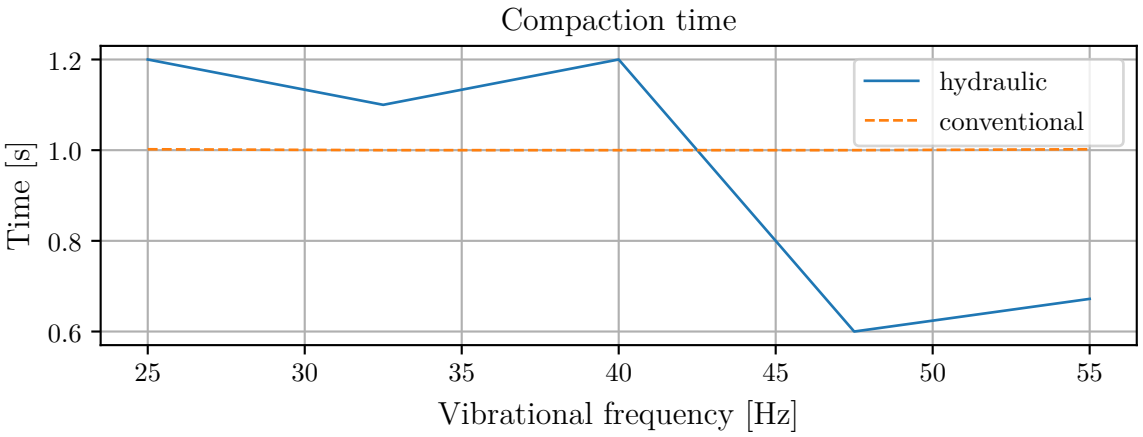

Figure 5.17: Compaction time for different vibrational frequencies.

The number of particles experiencing a force over 500 N and the force found in a CDF of the maximum force upon each particle at 99.99 % as functions of the vibrational frequency are shown in Figure 5.18 for both tamping models.

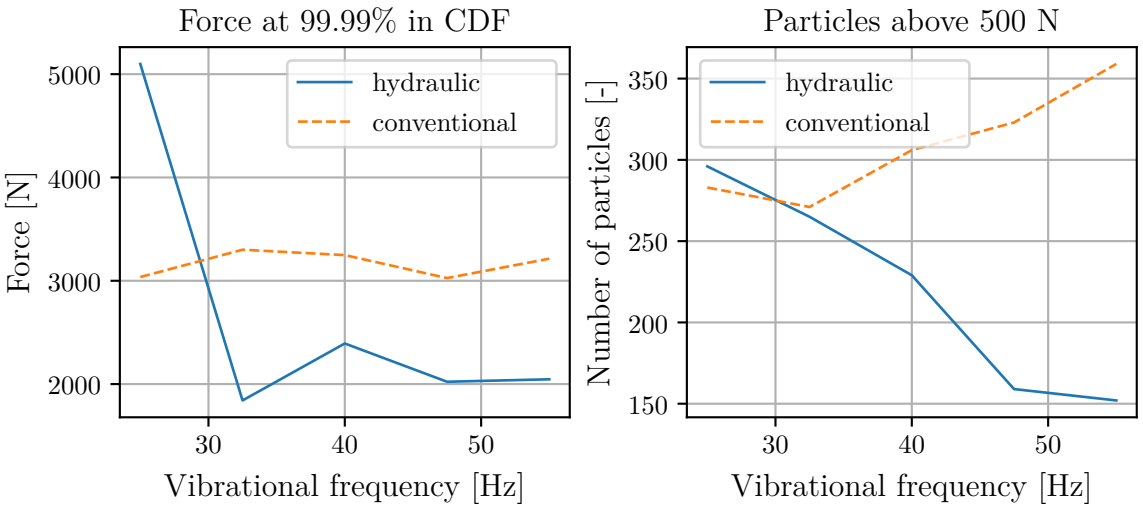

Figure 5.18: Forces acting upon particles for different vibrational frequencies.

For the fully hydraulic model, a frequency of 20 Hz gives very large forces from the CDF. For all other frequencies, along with all frequencies for the conventional model, the forces from the CDF are relatively constant. The force level is roughly 50 % higher for the conventional tamping model. The number of particles above

500 N decreases as the frequency increases for the fully hydraulic model. For the conventional model, the number of particles above 500 N increases with the frequency instead. These observed differences may be due to the difference in compaction time for the fully hydraulic model.

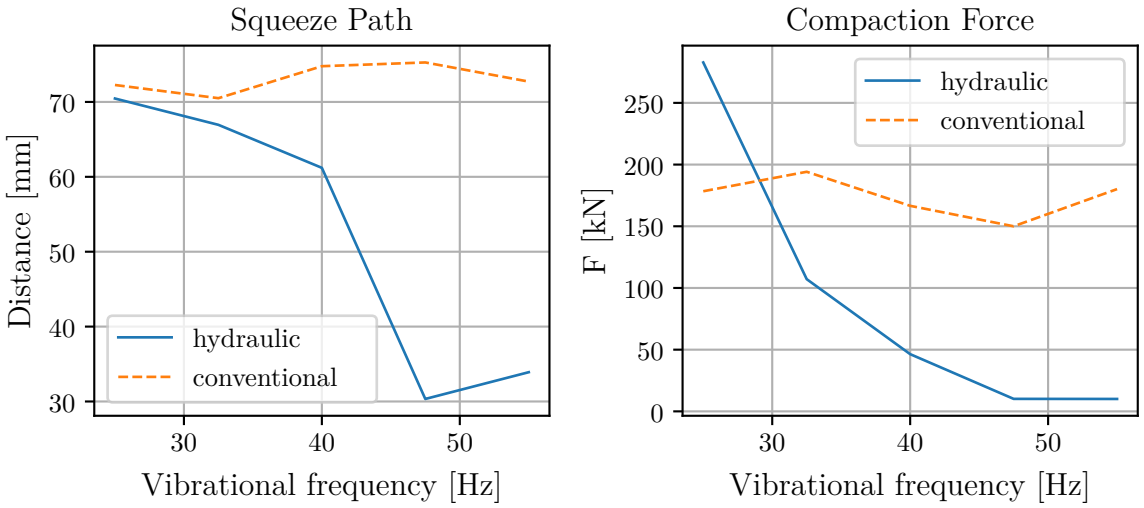

Figure 5.19: Squeeze path and compaction force for different vibrational frequencies.

The compaction force and squeeze path for both the hydraulic and the conventional tamping models are seen in Figure 5.19. For the conventional tamping model, the vibrational frequency does not have a large impact on the squeeze path or the compaction force, both of which are almost constant. For the fully hydraulic model, both the squeeze path and the compaction force decrease as the frequency increases. This behaviour may be attributed to the lower compaction time for higher frequencies.

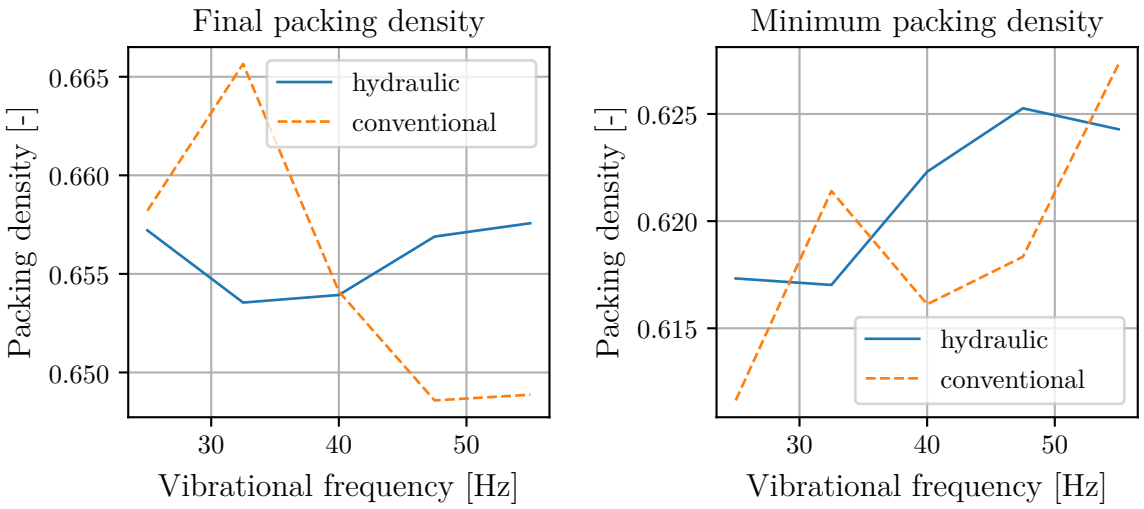

Figure 5.20: Final and minimum packing density for different vibrational frequencies.

The final and the minimum packing density for both the hydraulic and the conventional tamping models are seen in Figure 5.20. For the fully hydraulic tamping

model, the final packing density remains relatively constant for different frequencies, regardless of when or if the packing density criterion is reached. The final packing density decreases for higher vibrational frequencies for the conventional model. The minimum packing density generally increases with the frequency for both tamping models, showing that a higher vibrational frequency disturbs the ballast bed less upon insertion of the tamping tines.

6
Conclusions

In this section, conclusions related to the comparison of the fully hydraulic and the conventional tamping models are drawn in Section 6.1 while conclusions from the parameters study are given in Section 6.2. Section 6.3 answers the previously posed research questions. Finally, a number of proposals for future work related to the project are seen in Section 6.4.

6.1 Comparison

The comparison between the fully hydraulic and the conventional tamping model presented in Section 5.3 shows that the hydraulic tamping model is able to compact the ballast bed underneath the middle sleeper to a higher packing density than the conventional tamping model. This is true even though the tamping cycle of the fully hydraulic tamping model is shorter. The ballast to the side of the sleeper, where the tines are penetrated, is disturbed to a lesser degree by the fully hydraulic model. Analysis of the histogram and CDF of maximum force acting upon the particles reveals that the conventional tamping model exerts a higher level of force upon the ballast bed particles, potentially leading to more particle breakage of the ballast particles. Based on these results, it is concluded that the fully hydraulic tamping model is able to achieve a more compacted ballast bed underneath the middle sleeper while simultaneously ensuring a lower level of force upon the ballast particles as compared to the conventional tamping model.

6.2 Parameter Study

For the vibrational amplitude, the results of the parameter study reveal the following: for the conventional tamping model, higher amplitude values give higher compaction force, squeeze path and forces acting upon the ballast particles. However, amplitudes above 3.5 mm yield a higher packing density underneath the middle sleeper, with a maximum found at 5 mm. The nominal value for the vibrational amplitude of 5 mm yields the minimum force at 99.99% in the CDF while simultaneously reaching the highest packing density underneath the sleeper. This result points toward the nominal vibrational amplitude being the optimal point for the conventional tamping model. However, further studies of the effects of the vibrational amplitude may be required to confidently ascertain this statement. For the fully hydraulic tamping model, the compaction time has a significant influence on the results. For amplitudes under 5 mm, the packing density criterion is not reached

and the compaction time is 1.2 s. For these amplitude values, the forces upon the particles, along with the compaction force and squeeze path, are significantly higher than for amplitudes of 5 mm or higher. This points towards a higher degradation of the ballast bed as a result of a longer tamping operation. Amplitudes of 5 mm or higher provide similar magnitudes in the forces acting upon particles, though the minimum is found at 5 mm. The packing density increases with the vibration amplitude. The optimal vibrational amplitude for the fully hydraulic model seems to be located at 5 mm, however, a higher amplitude may yield a higher final packing density at a slight increase in the forces acting upon the ballast particles.

For the vibrational frequency, the parameter study shows that the frequency has varying levels of impact on the results. For the conventional tamping model, only small differences may be observed for the compaction force, squeeze path and the value at 99.99 % in a CDF. The number of particles above 500 N and the minimum packing density increases slightly with a higher frequency, while the final packing density decreases. These results show that the effects of the vibrational frequency are not very large, however, lower vibrational frequencies seem to yield lower force upon particles and a higher final packing density. For the fully hydraulic tamping model, the compaction time is high for frequencies of 40 Hz and below, while it is low for higher frequencies. This difference in compaction time has a significant impact on the results of the parameter study. The forces on the particles, along with the squeeze path and compaction force, all decrease significantly as the vibrational frequency increases. The minimum packing density increases with the frequency, while the final packing density stays relatively constant. These results show that a higher vibrational frequency for the fully hydraulic tamping model manages to significantly decrease the forces upon the ballast particles and the tamping tines, while maintaining the same final packing density as the lower vibrational frequencies.

6.3 Summary Of Findings

- *How may the two tamping processes be modeled in a DEM-MBD co-simulation framework?*
  Using Demify® and Simulink, the two tamping processes may be modeled according to the methodology described in Chapter 3.

- *How may the results of the tamping process be quantified in a manner that properly exploits the strengths found in a DEM-MBD co-simulation as compared to real-world experiments?*
  By examining the packing density found underneath the middle sleeper along with the distribution of forces upon the ballast particles, the results of the tamping process may be evaluated. Retrieving these results from the DEM simulation is simple, while retrieving the same results from a real-world experiment is highly difficult, if not impossible.

- *In what way do the two tamping processes vary in terms of the previously mentioned quantifiable results?*
  The fully hydraulic tamping model proved to be able to achieve a higher packing density underneath the middle sleeper while maintaining lower levels of force upon the ballast particles as compared to the conventional tamping model.

- *In what way do the results of the tamping process change with varying values of critical tamping design parameters?*
  For the vibrational amplitude: The optimal value seems to be found at 5 mm for both tamping models. A higher amplitude may however provide some advantages for the fully hydraulic tamping model.
  For the vibrational frequency: Lower frequencies shows to have some advantages for the conventional tamping model, while the higher frequencies gives significant improvements to the fully hydraulic tamping model.

6.4 Future Work

Aspects for future work related to the project are seen below.

- Introduction of a particle breakage model may provide further insights into how the tamping operation affects the condition of the ballast bed. It may also be possible to evaluate which mechanisms cause the particle breakage.
- Further expansion of the parameter study to include additional design parameters may yield more insight into how the tamping operation is affected by said parameters.
- Optimization of design parameters, either to ensure that the nominal values that are typically used for a tamping machine are the optimal values or to find some other values/combination of values that may provide a better result.
- Expanding the computational domain to include additional sleepers in order to investigate the effects of the tamping tine vibrations on the ballast particles further away from the middle sleeper.
- Expanding the computational domain to include the subballast.
- Modeling the fastening system between rail and sleeper to allow for movement of the sleeper due to forces from the tamping operation.
- Using a pre-compacted ballast bed for the tamping model to investigate how the tamping operation affects the packing density for an initial ballast bed with a higher packing density.
- Conducting a more thorough time step verification of the DEM simulation to ensure that the chosen time step is sufficiently small.

Bibliography

[1] Trafikverket, "Järnkoll på tågresor," 2023.

[2] Trafikverket, "Järnkoll på spåren," 2023.

[3] Y. Guo, V. Markine, and G. Jing, "Review of ballast track tamping: Mechanism, challenges and solutions," *Construction and Building Materials*, vol. 300, p. 123940, Sept. 2021.

[4] B. Lichtberger, *Track compendium*. Hamburg: Eurailpress, 2011.

[5] S. Shi, L. Gao, X. Cai, Y. Xiao, and M. Xu, "Mechanical characteristics of ballasted track under different tamping depths in railway maintenance," *Transportation Geotechnics*, vol. 35, p. 100799, July 2022.

[6] O. Barbir, *DEVELOPMENT OF CONDITION-BASED TAMPING PROCESS IN RAILWAY ENGINEERING - Operating Phases and Motion Behavior, Ballast Condition Determination, Ballast fluidization.* PhD thesis, 2022.

[7] R.L., "Geleisetopf-maschine system "scheuchzer"," 1938.

[8] P. A. Cundall and O. D. L. Strack, "A discrete numerical model for granular assemblies," *Géotechnique*, vol. 29, pp. 47–65, Mar. 1979.

[9] T. Zhou, B. Hu, J. Sun, and Z. Liu, "Discrete element method simulation of railway ballast compactness during tamping process," *The Open Electrical amp; Electronic Engineering Journal*, vol. 7, pp. 103–109, Nov. 2013.

[10] X. J. Wang, Y. L. Chi, W. Li, and T. Y. Zhou, "Study on the dem simulation of the granular railway ballast bed tamping," *Advanced Materials Research*, vol. 524–527, pp. 3256–3259, May 2012.

[11] S. Shi, L. Gao, X. Cai, H. Yin, and X. Wang, "Effect of tamping operation on mechanical qualities of ballast bed based on dem-mbd coupling method," *Computers and Geotechnics*, vol. 124, p. 103574, Aug. 2020.

[12] S. Shi, L. Gao, H. Xiao, Y. Xu, and H. Yin, "Research on ballast breakage under tamping operation based on dem–mbd coupling approach," *Construction and Building Materials*, vol. 272, p. 121810, Feb. 2021.

[13] Z. Zhang, H. Xiao, Y. Wang, Y. Chi, M. M. Nadakatti, and J. Jin, "Numerical simulation of the three-sleeper asynchronous tamping operation of ballast bed based on the virtual unit module and polyhedral ballast model," *Transportation Geotechnics*, vol. 40, p. 100964, May 2023.

[14] Y. Chi, H. Xiao, Z. Zhang, M. M. Nadakatti, and Z. Qian, "Analysis of the influence of vibration frequency and amplitude on ballast bed tamping operation in railway turnout areas," *Computational Particle Mechanics*, Sept. 2023.

[15] A. Bilock, "A gpu polyhedral discrete element method," Master's thesis, Chalmers University of Technology, 2020.

[16] MathWorks, "Simscape multibody."

[17] T. Blochwitz, M. Otter, M. Arnold, C. Bausch, C. Clauss, H. Elmqvist, A. Junghanns, J. Mauss, M. Monteiro, T. Neidhold, D. Neumerkel, H. Olsson, J.-V. Peetz, and S. Wolf, "The functional mockup interface for tool independent exchange of simulation models," in *Proceedings from the 8th International Modelica Conference, Technical Univeristy, Dresden, Germany*, Modelica, Linköping University Electronic Press, June 2011.

[18] "Pyfmu." `https://github.com/INTO-CPS-Association/pyfmu`, 2020.

[19] S.-E. 13231-1:2024, "Järnvägar - infrastruktur - godkännande av arbeten - del 1: Arbeten i ballasterade spår - spår, spårväxlar och spårkorsningar," standard, Svenska Institutet för Standarder, Jan. 2024.

[20] O. B. A. Bernhard, C. Koczwara, "Intelligent tamping – from research to automation," *PWI*, vol. 140 Pt3, 2022.

[21] B. Lichtberger, "Tamping technologies and their impact on track durability," *ZEV Glasers Annalen*, vol. 8, 2023.

[22] H. Zhu, Z. Zhou, R. Yang, and A. Yu, "Discrete particle simulation of particulate systems: Theoretical developments," *Chemical Engineering Science*, vol. 62, pp. 3378–3396, July 2007.

[23] C. Shi, Z. Fan, D. P. Connolly, G. Jing, V. Markine, and Y. Guo, "Railway ballast performance: Recent advances in the understanding of geometry, distribution and degradation," *Transportation Geotechnics*, vol. 41, p. 101042, July 2023.

[24] K. Buist, L. Seelen, N. Deen, J. Padding, and J. Kuipers, "On an efficient hybrid soft and hard sphere collision integration scheme for dem," *Chemical Engineering Science*, vol. 153, pp. 363–373, Oct. 2016.

[25] H. HERTZ, "On the contact of elastic solids," *Z. Reine Angew. Mathematik*, vol. 92, pp. 156–171, 1881.

[26] B. Nye, A. V. Kulchitsky, and J. B. Johnson, "Intersecting dilated convex polyhedra method for modeling complex particles in discrete element method," *International Journal for Numerical and Analytical Methods in Geomechanics*, vol. 38, pp. 978–990, May 2014.

[27] S.-E. 13450, "Makadamballast för järnväg," standard, Svenska Institutet för Standarder, Feb. 2003.

[28] MathWorks, "Modeling a double-acting actuator."

[29] M. Marigo and E. H. Stitt, "Discrete element method (dem) for industrial applications: Comments on calibration and validation for the modelling of cylindrical pellets," *KONA Powder and Particle Journal*, vol. 32, no. 0, pp. 236–252, 2015.

DEPARTMENT OF INDUSTRIAL AND MATERIALS SCIENCE
CHALMERS UNIVERSITY OF TECHNOLOGY
Gothenburg, Sweden
www.chalmers.se

CHALMERS
UNIVERSITY OF TECHNOLOGY